
Temperature-controlled vacuum quenching for perovskite solar modules towards scalable production

In the format provided by the authors and unedited

Table of contents

Supplementary note I. Three stages in the vacuum quenching.

Supplementary note II. Antoine equation: to predict the boiling point at different pressures.

Supplementary Fig. 1. Vacuum quenching equipment.

Supplementary Fig. 2. Wavelength variation In-situ PL of three popular nucleation methods.

Supplementary Fig. 3. Photos and XRD patterns of Films after quenching before annealing.

Supplementary Fig. 4. SEM of spin and blade-coated films by three nucleation methods after annealing.

Supplementary Fig. 5. XRD patterns of annealed films fabricated by different quenching methods.

Supplementary Fig. 6. In-situ PL heat map of different vacuum quenching speeds.

Supplementary Fig. 7. The correlation between boiling points and pressure of different solvents used in perovskite precursor.

Supplementary Fig. 8. Pressure change of different solvent systems during vacuum treatment.

Supplementary Fig. 9. In-situ PL study of different Main solvents with different boiling points during vacuum quenching.

Supplementary Fig. 10. In-situ PL study of different Lewis bases during vacuum quenching.

Supplementary Fig. 11. In-situ PL study of different additives during vacuum quenching.

Supplementary Fig. 12. In-situ PL study of different bandgaps.

Supplementary Fig. 13. Temperature changes during antisolvent and vacuum quenching.

Supplementary Fig. 14. The temperature change of the glass substrate before and after it was placed on the temperature control platform inside the vacuum quenching equipment.

Supplementary Fig. 15. The peak wavelength of in-situ PL changes with time during vacuum

quenching at different temperatures.

Supplementary Fig. 16. In-situ PL intensity of different temperatures during vacuum quenching of DMF: NMP precursor system.

Supplementary Fig. 17. Photos of films obtained by vacuum quenching at different temperatures.

Supplementary Fig. 18. Photoluminescence spectrum of annealed film after different T-VAQ treatments.

Supplementary Fig. 19. Statistical plots of PSCs at different vacuum quenching temperatures.

Supplementary Fig. 20. In-situ PL study of different temperatures during vacuum quenching with the DMF: DMSO precursor system.

Supplementary Fig. 21. In-situ PL study of control film and film with *p*F-PEAI during annealing.

Supplementary Fig. 22. Scanning electron microscope (SEM) of control film and the film with *p*F-PEAI.

Supplementary Fig. 23. X-ray photoelectron spectroscopy (XPS) study of control film and the film with *p*F-PEAI.

Supplementary Fig. 24. SEM images of the cross-section of the PSM.

Supplementary Fig. 25. EQE of perovskite solar cell.

Supplementary Fig. 26. Statistical plots of PSCs at antisolvent and vacuum quenching methods.

Supplementary Fig. 27. Statistical plots of PSMs at antisolvent and vacuum quenching methods.

Supplementary Fig. 28. Laser patterning of the PSM.

Supplementary Fig. 29. Certification report.

Supplementary Fig. 30. Uniformity test of antisolvent and T-VAQ treated film by PL and UV.

Supplementary Fig. 31. Uniformity of T-VAQ treated film by SEM.

Supplementary Fig. 32. $J-V$ of $p-i-n$ structure mini-module with the perovskite film fabricated by a blade-coating and T-VAQ method.

Supplementary Fig. 33. $J-V$ of $n-i-p$ structured mini-module with the perovskite film fabricated by vacuum quenching method.

Supplementary Fig. 34. $J-V$ of $p-i-n$ structured wide-bandgap PSCs with the perovskite film fabricated by vacuum quenching method.

Supplementary table 1. Quantitative evaluation of three quenching methods: antisolvent, vacuum, and gas quenching.

Supplementary table 2. Antoine coefficients of solvents widely used in perovskite photovoltaics.

Supplementary table 3. Donor number and boiling point of different main solvents.

Supplementary table 4. Wavelength variation of in-situ PL of vacuum quenching at different temperatures.

Supplementary table 5. Statistic photovoltaic parameters of the T-VAQ-based PSCs at different temperatures with an active area of 0.04 cm^2 .

Supplementary table 6. Statistic photovoltaic parameters of the antisolvent and T-VAQ-based solar cells (0.04 cm^2) and mini-modules (11.0 cm^2).

Supplementary table 7. Width of Sub-cell and each laser scribing of the PSMs.

Supplementary note I. Three stages in vacuum quenching.

The vacuum process can be divided into three stages. The first stage only extracts air from the vacuum chamber. In contrast, the second stage starts with extracting solvent from the film. The extracted solvent was considered to have no interaction with the solute since the concentration of solutes in the wet film was relatively low. In the third stage, the interaction between solutes and solvents cannot be ignored. With the concentration of solutes gradually increasing, the film begins to supersaturate and nucleate.

First stage:

In the first stage, the vacuum pump only extracts the atmosphere inside the chamber. Since the vacuum degree has not yet reached a point where the boiling point of the solvent is lower than room temperature and the solvent has not boiled, the influence of the solvent can be ignored. When applying some approximate conditions in this process, Assumption 1: The pumping speed of a pump from 760 Torr to 10 mTorr maintains constant, denoted as S . Assumption 2: There is no air leakage in the system. Assumption 3: The process is isothermal. Assumption 4: The pump is directly connected to the vacuum chamber, with infinite flow conductivity.

The variation law of system pressure over time could be as follows:

$$P(t) = P(0)e^{-\frac{St}{V}}$$

S is the pumping speed, V is the volume of the chamber, and t is the pumping duration. This function could indicate the chamber pressure after pumping for a certain duration. According to this formula, pressure is a logarithmic function of time (Fig. 3B). When the pumping speed of the pump is higher, the pressure in the vacuum chamber will decrease faster, thereby achieving the vacuum degree at which the solution boils at room temperature in a shorter time.

According to this function, the pumping speed of the pump can be selected:

$$S = \frac{V}{t} \ln \frac{P_0}{P_1} = \frac{2.3V}{t} \lg \frac{P_0}{P_1}$$

After determining the volume and flow resistance of the vacuum system, the pumping speed of the pump can be selected based on the solvent system used to prepare the perovskite and the area of the film to be processed.

Second stage:

Low boiling point (b.p.) solvents evaporate first in the second stage. Since the solute in the perovskite precursor has not yet reached supersaturation, the interaction between the perovskite precursor component and the solvent is relatively weak. Assumption 5: The system extracts pure solvent in the second stage. As shown in Supplementary Fig. 7, the specific b.p. at different air pressures is determined by the Antoine equation and the inherent properties of the solvent. Please refer to the supplementary text (Antoine equation to predict the boiling point at different pressures) for specific formulas and solvent parameters (Supplementary Table 2). Taking DMF as an example, when the system pressure drops to 2.7 Torr, DMF will reach its boiling point at 20 °C and rapidly escape from the perovskite precursor film.

In a mixed solvent system, the concentration of molecules per unit volume is reduced, which decreases the number of solvent molecules that can escape from the liquid surface into the gas phase per unit time. As a result, the solvent and its vapor pressure can reach equilibrium at a lower vapor pressure than the pure solvent. In other words, the vapor pressure of the solvent in the mixed solution is lower than that of the pure solvent. This observation aligns with Raoult's law:

$$p_A = p_A^* \frac{n_A}{n_A + n_B}$$

where p_A is the partial pressure of the component A in the gaseous mixture above the solution, p_A^* is the equilibrium vapor pressure of the pure component A , and n_A and n_B are the mole of the component A and B in the liquid solution.

To satisfy the above conditions, the interaction force between solvents A and B must equal the interaction force within each solvent. However, this is not always the case in reality. Therefore, activity (a_A) and the activity coefficient (γ_A) are introduced to adjust Raoult's law accordingly.

$$a_A = \gamma_A \frac{n_A}{n_A + n_B} = \gamma_A \frac{p_A}{p_A^*}$$

The more dilute the real solution, the closer the solvent's activity coefficient approaches 1, making the activity and molar fraction nearly equal, indicating behavior more akin to an ideal solution. During vacuum quenching, as the solute concentration increases in step 3, the interactions between the solute and solvent become more pronounced, causing the molar fraction to no longer accurately represent the solvent's activity. Although we did not obtain quantitative measurements of the solvent's activity at different stages, this information can still provide valuable qualitative insights into the changes occurring in the system during vacuum quenching.

In Figure 3E, we added 5 μL of various solvents to the vacuum chamber to verify the above theoretical analysis. We found that in the initial stage, the pressure curves of different solvents were consistent with each other and showed a sharp decrease trend. However, after approximately 5 seconds, the curves with added solvents displayed an increased pressure compared to the control group. The DMF curve began to rise at around 300 mTorr, DMSO was around 100 mTorr, and NMP showed a significant change at about 70 mTorr. This phenomenon

is consistent with the trend of the boiling point of solvents. Regarding the mixed solvent, we measured the system of DMF: DMSO = 4:1, as shown in Supplementary Fig. 8. The pressure curve obtained by extracting the mixed solvent coincides with the linear superposition of two curves of DMF and DMSO together.

Third stage:

At this stage, the concentration of the precursor film becomes higher, and the interaction between the solvent and the perovskite components cannot be overlooked. The precursor film undergoes a transition from unsaturated to supersaturated. The ratio of perovskite to solvent approaches 1:3.4 (or 3.8M).¹

The third stage is the most crucial stage for perovskite nucleation. It requires the highest pump speed among the three stages. How the pressure is reduced determines how and at what speed the system enters the supersaturation process. The pressure and pumping speed of the three stages can be achieved by controlling the pumping path, such as using a low-pressure vacuum tank to reduce the pressure of the vacuum chamber for a short period to achieve rapid nucleation.

In the third stage, the binding effect of the perovskite solute on the solvent becomes increasingly evident, which is reflected in physical quantities as the saturation vapor pressure of the solvent decreases. It is speculated that its saturated vapor pressure becomes relatively low, making it difficult to be removed directly by the pump. To achieve faster supersaturation, the donor number of the solvent can determine the interaction strength between the solvent and the perovskite solute to optimize the third stage (Supplementary Table 1).

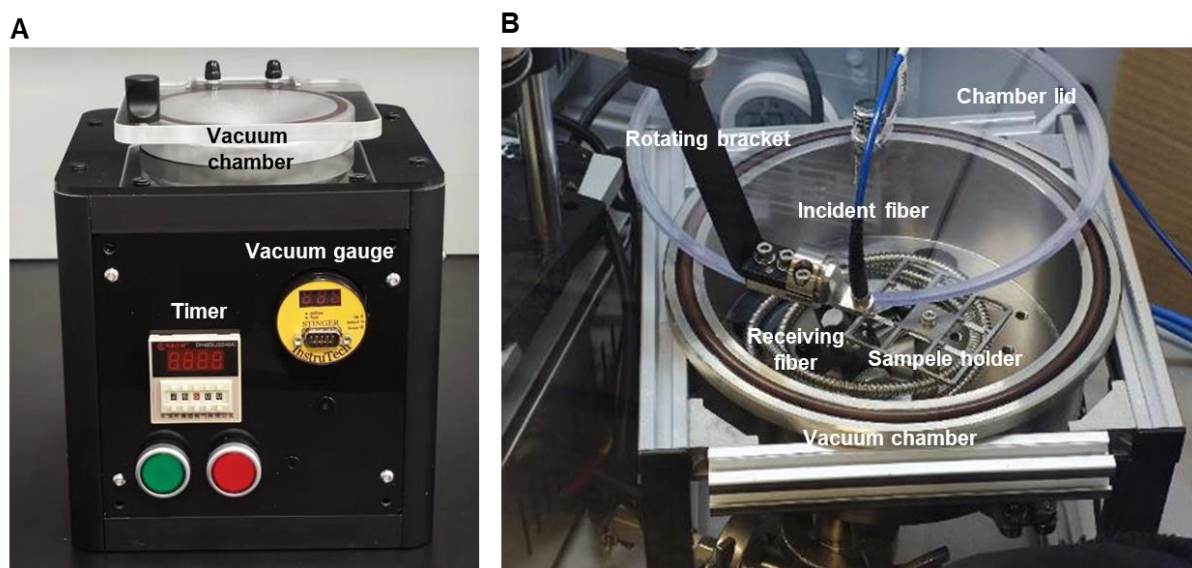
Supplementary note II. Antoine equation: to predict the boiling point at different pressures.

$$\log_{10}(P^*) = A - \frac{B}{T + C}$$

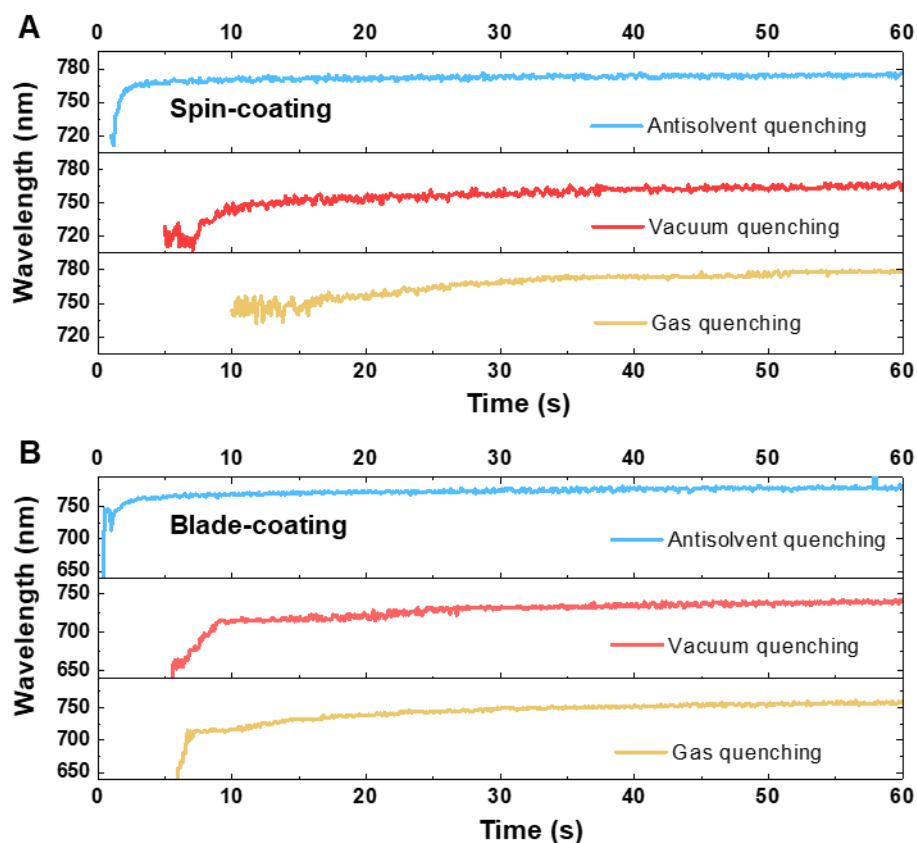
where P is pressure in mmHg and T is temperature in Celsius, A , B and C are Antoine coefficients related to solvents, $T_{\min} < T < T_{\max}$.

Through this formula, we can predict the Pressure change of different solvent systems during vacuum quenching. In general, as shown in Supplementary Fig. 7, the lower the gas pressure, the lower the boiling point of the solvent. Vacuum quenching uses this principle to make the solvent escape from the perovskite film at environment temperature. The Antoine coefficients of several commonly used solvents can be found in Supplementary Table 2. The data source is the Antoine coefficients for vapor pressure' chart from the Iranian chemical engineers website.²

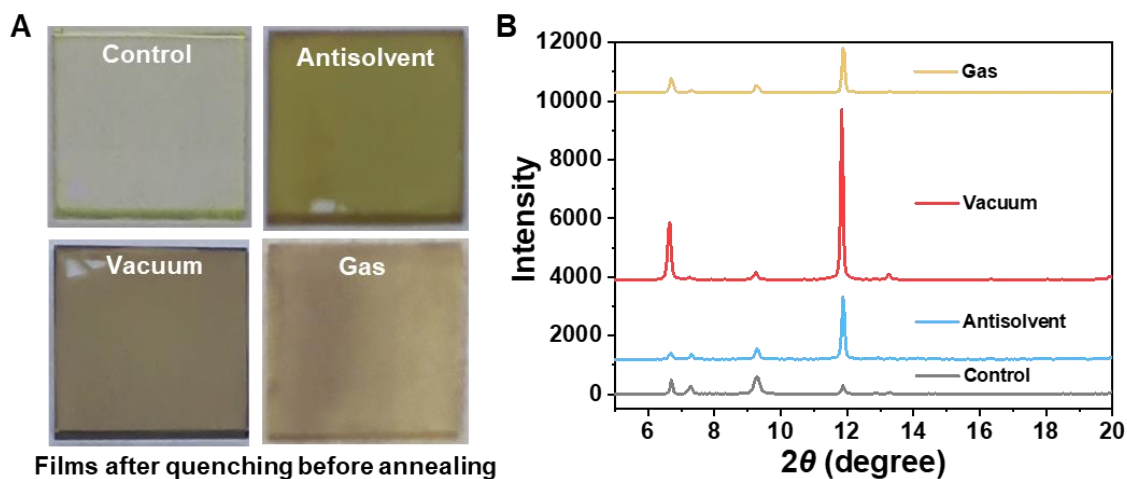
Supplementary figures.



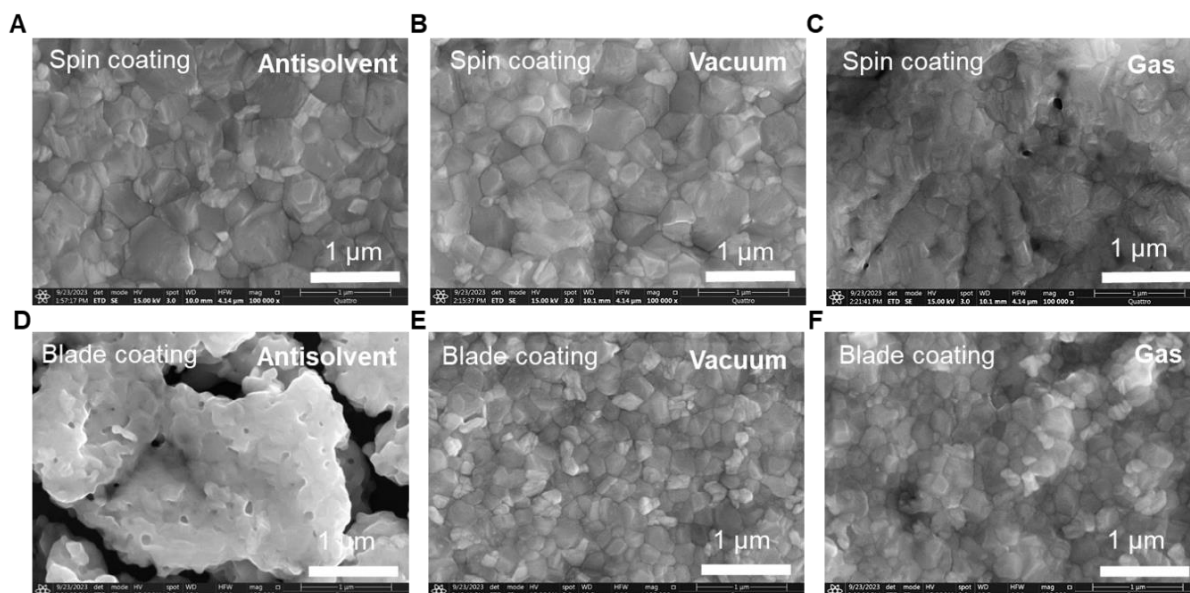
Supplementary Fig. 1. Vacuum quenching equipment. (A) The compact vacuum quencher used in the glove box, with a transparent chamber lid to monitor the film color, a vacuum gauge to monitor the pressure and a timer to control the quenching duration. (B) The in-situ PL integrated vacuum quencher. The incident fiber could move in a circular path by the rotating bracket. This device can prevent the incident light from continuously shining in the same position at the wet perovskite film during the test. These devices were developed with technical support from Solvert Tech. Co., Ltd.



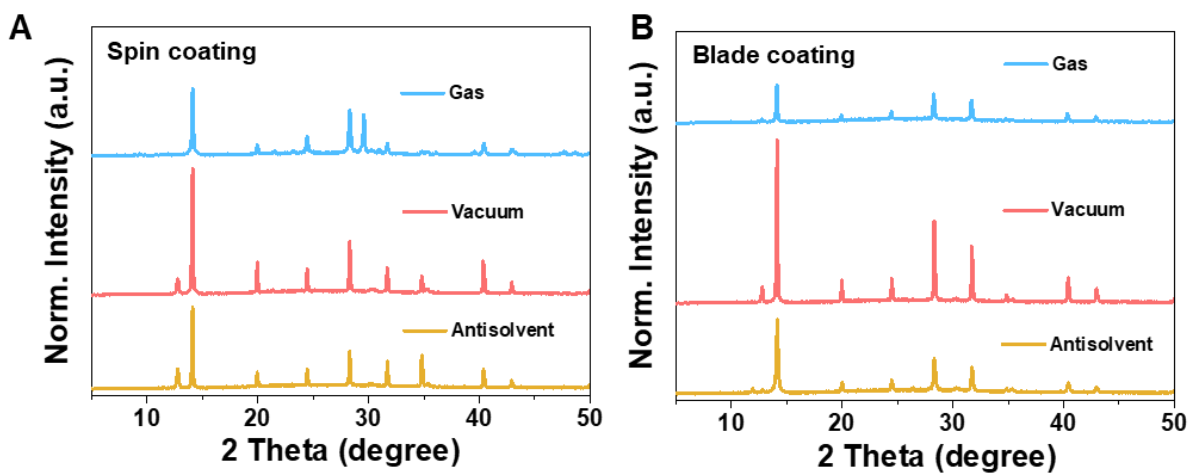
Supplementary Fig. 2. Wavelength variation In-situ PL of three popular nucleation methods. Wavelength variation In-situ PL of three popular nucleation methods in (A) spin-coating method and (B) blade-coating method. The wavelength red shifting was observed in all lines. This shifting relates to the MACl, as discussed in the previous publication³ and **Supplementary Fig. 11**. In both spin-coating and blade-coating groups, antisolvent quenching samples show the PL signal in its first 2 seconds, then shift to > 750 nm within 3 seconds. Vacuum quenching and gas quenching methods show slower peak emergency and shifting, indicating the different quenching abilities.



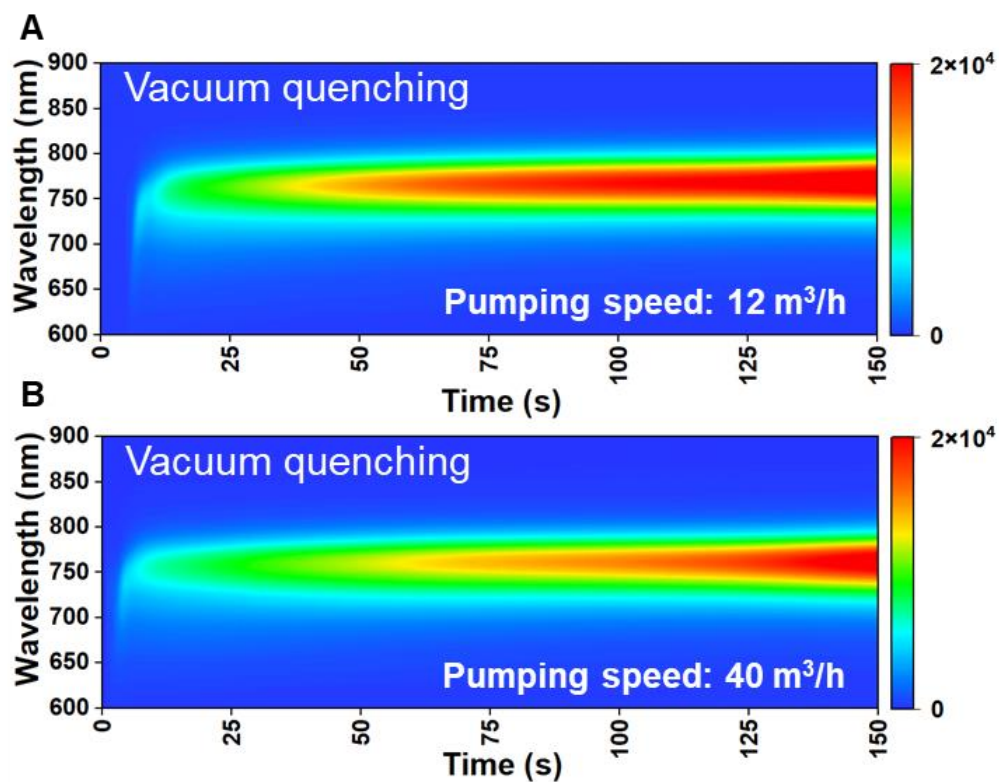
Supplementary Fig. 3. Photos and XRD patterns of Films after quenching before annealing. (A) Photos of films in three nucleation methods and (B) XRD of films in three nucleation methods without annealing. The control film was transparent and almost colorless. The antisolvent and vacuum-quenched films were transparent and showed a yellow-to-brown color. In contrast, the gas-quenched film was semitransparent with an uneven color. All samples show a similar intermediate phase. The vacuum-quenched film shows the highest XRD peaks, indicating good crystallinity of the intermediate phase after vacuum-quenching treatment.



Supplementary Fig. 4. SEM of spin and blade-coated films by three nucleation methods after annealing. (A, B, C) Spin-coated films by three quenching methods. The antisolvent film shows a similar morphology to the vacuum quenched film, indicating that the well-studied perovskite formula by the antisolvent quenching method can be directly transplanted to the vacuum quenching method. The gas-quenched film shows obvious pinholes in the film and relatively uneven morphology. The gas quenching method requires the perovskite precursor to be removed more easily. (D, E, F) Blade-coated films by three quenching methods. The antisolvent bath quenching method results in a rough surface, which may result from the too-fast quenching speed combined with the Fig. 2H blue line. As a result, the solute cannot move in time, resulting in many voids. The antisolvent bath is relatively difficult to control because of its fast quenching speed. It is hard to remove the solvent quickly, resulting in a prolonged quenching process. Vacuum-quenched film shows a uniform grain size. The gas-quenched film shows a relatively uneven surface than the vacuum-quenched film.

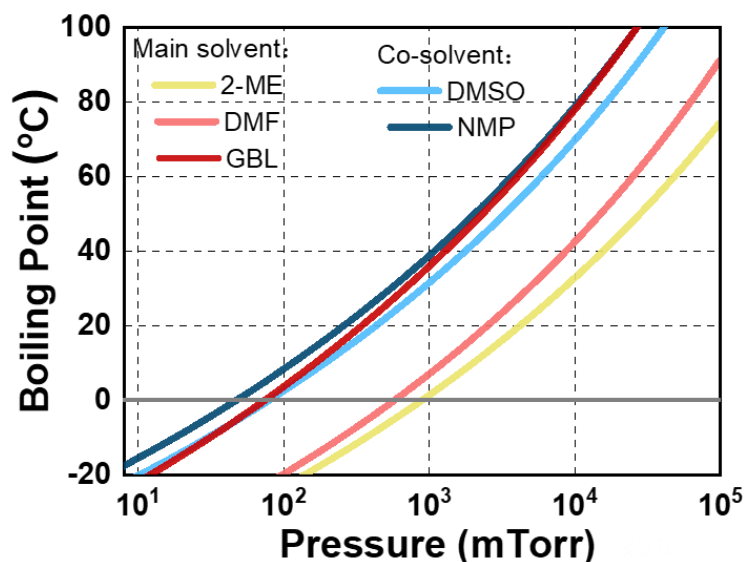


Supplementary Fig. 5. XRD patterns of annealed films fabricated by different quenching methods. (A, B) XRD of (A) spin-coated and (B) blade-coated films by three nucleation methods after annealing. Vacuum-quenched film shows the strongest XRD signal among the three treatments.

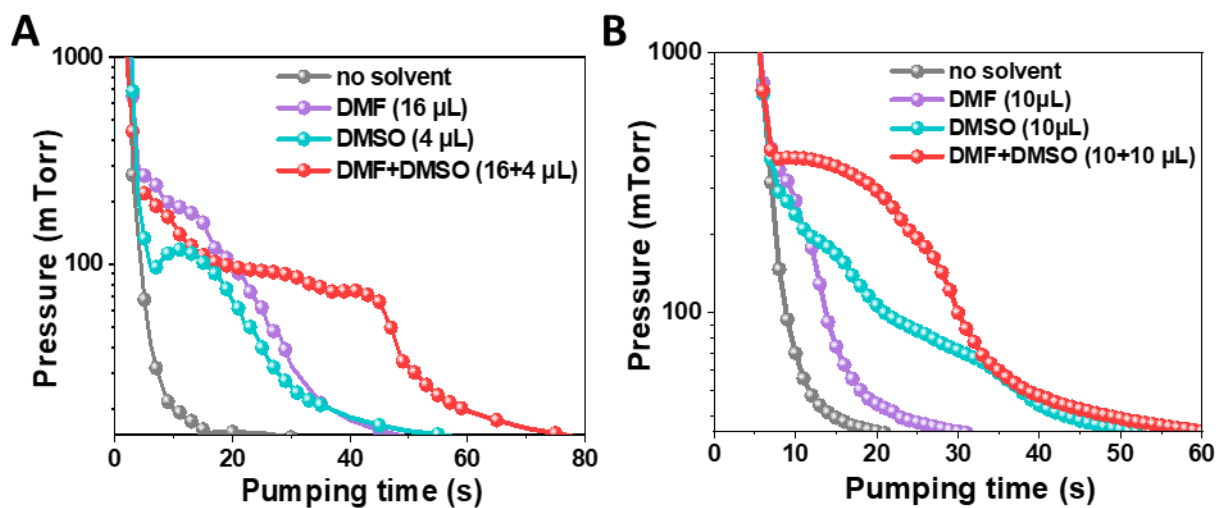


Supplementary Fig. 6. In-situ PL heat map of different vacuum quenching speeds. (A, B)

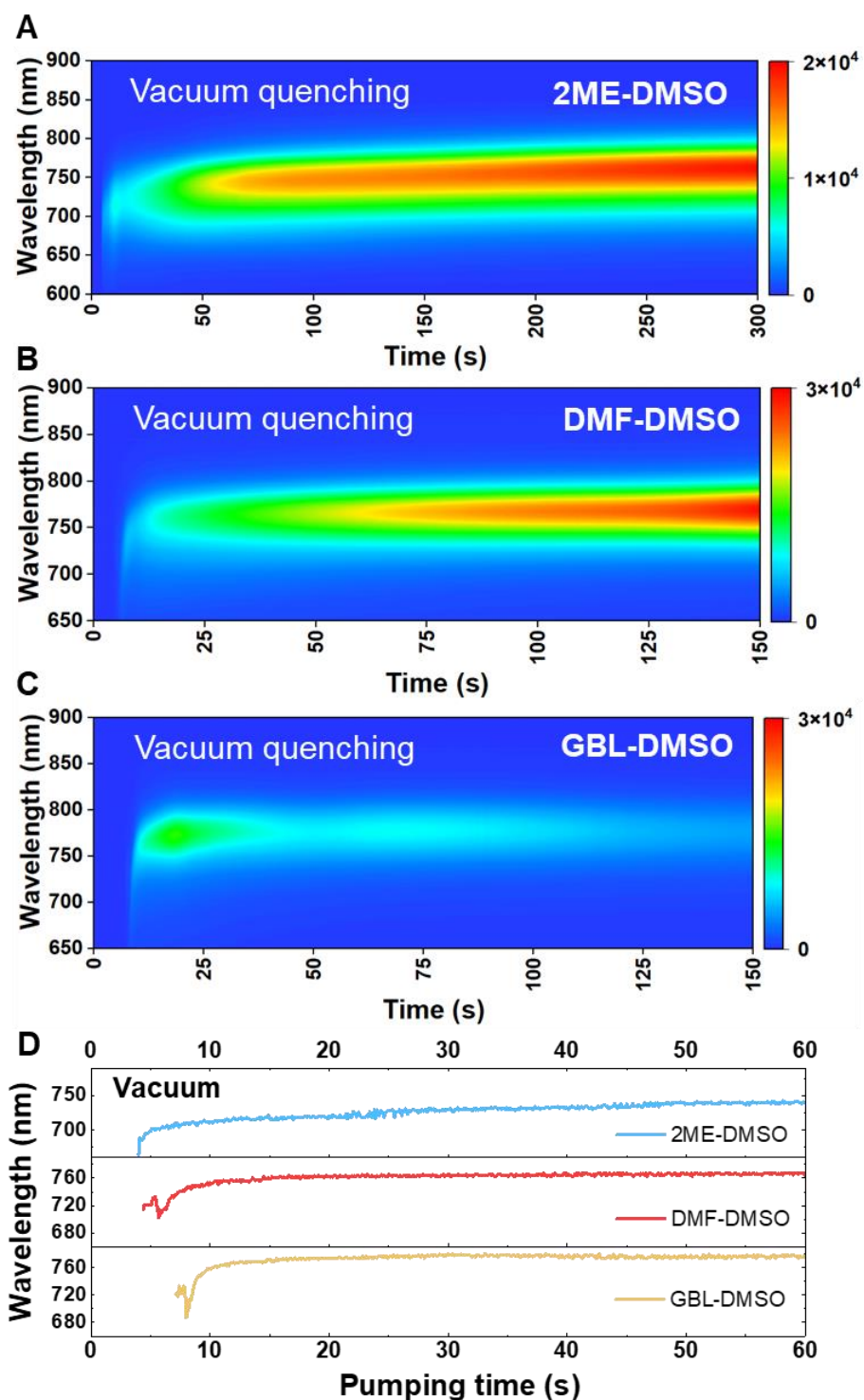
In-situ PL heat map of different vacuum quenching speeds. A stronger pump leads to faster nucleation of wet perovskite film. Combining real-time air pressure data, the PL peak appears when the vacuum degree is lower than 500 mTorr.



Supplementary Fig. 7. The correlation between boiling points and pressure of different solvents used in perovskite precursor. The boiling points (b.p.) of various solvents decrease with the decrease of air pressure. The specific b.p. at different air pressures is determined by the Antoine equation and the inherent properties of the solvent. Please refer to the supplementary text for specific formulas and solvent parameters (Supplementary Table 2). Taking DMF as an example, when the system pressure drops to 2.7 Torr, DMF will reach its boiling point at 20 °C and rapidly escape from the perovskite film.

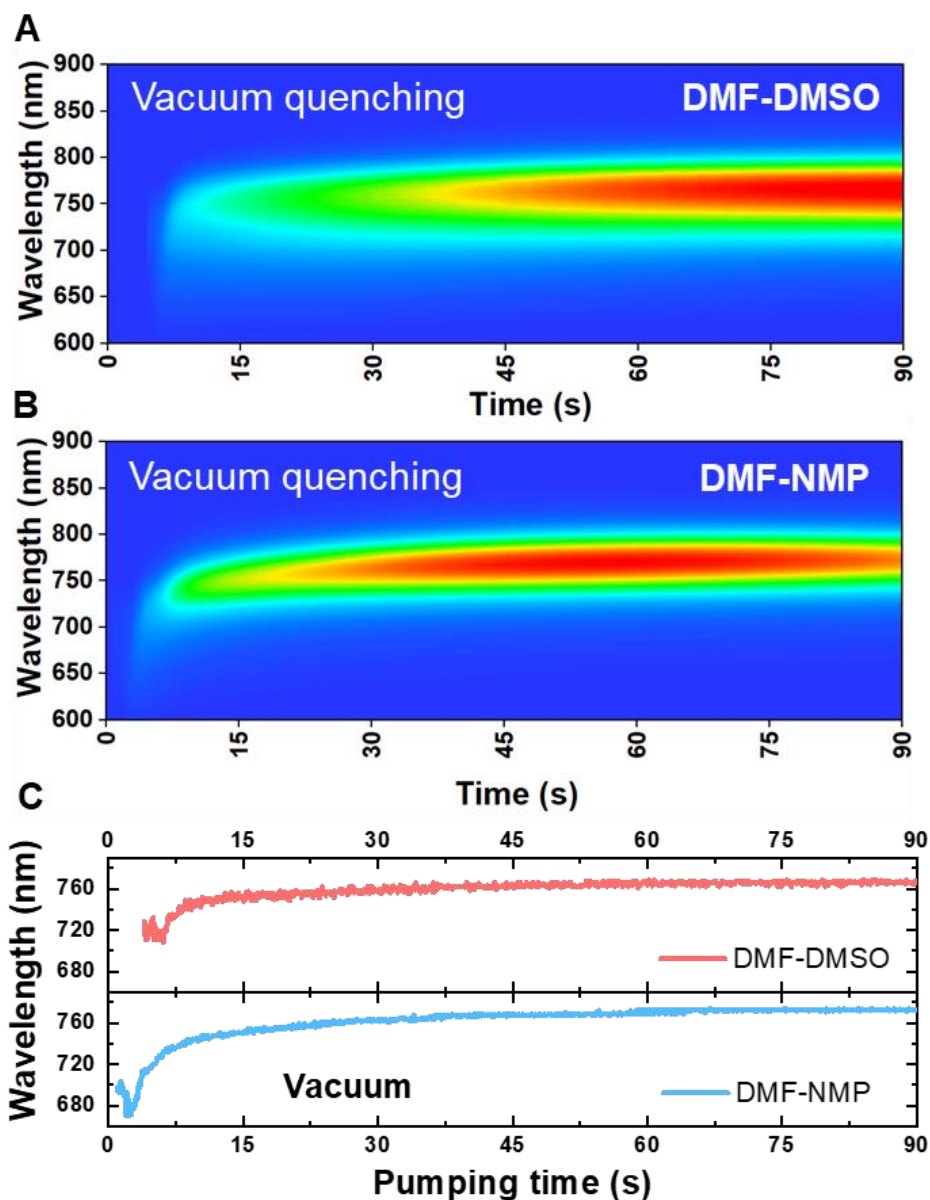


Supplementary Fig. 8. Pressure change of different solvent systems during vacuum treatment. In a fixed vacuum quenching system, a different solvent was added to the chamber to study the pressure behavior during the vacuum treatment. (A) DMF (16 μL), DMSO (4 μL) and DMF+DMSO (16+4 μL). (B) DMF (10 μL), DMSO (10 μL) and DMF+DMSO (10+10 μL).

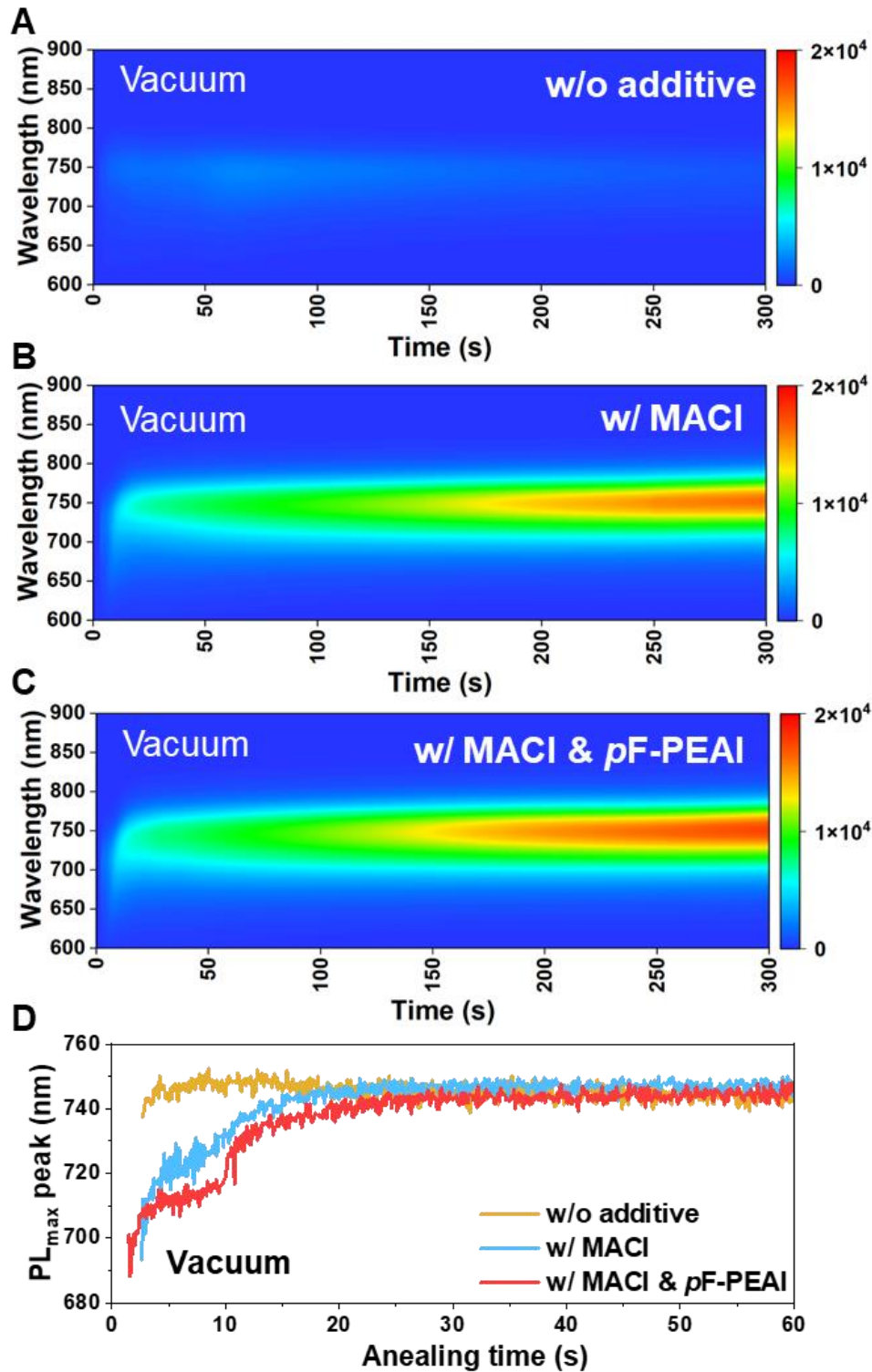


Supplementary Fig. 9. In-situ PL study of different Main solvents with different boiling points during vacuum quenching. In-situ PL was applied to monitor the nucleation period under vacuum quenching of different precursor solvent systems: (A) 2ME-DMSO, (B) DMF-DMSO, and (C) GBL-DMSO. (D) Wavelength variation In-situ PL in A, B and C. Step II is the

main difference in this comparison group. The solvents require different pressures at room temperature to evaporate (Supplementary Fig. 7). So, for the high boiling point solvent, the vacuum chamber needs to reach a lower air pressure for the solvent to evaporate. Meanwhile, high boiling point solvents of the same volume will achieve a larger equivalent volume at lower pressure. Therefore, high boiling solvents require a longer time to be extracted. As a result, GBL (204 °C) takes more time than DMF (153 °C) than 2ME (124 °C).



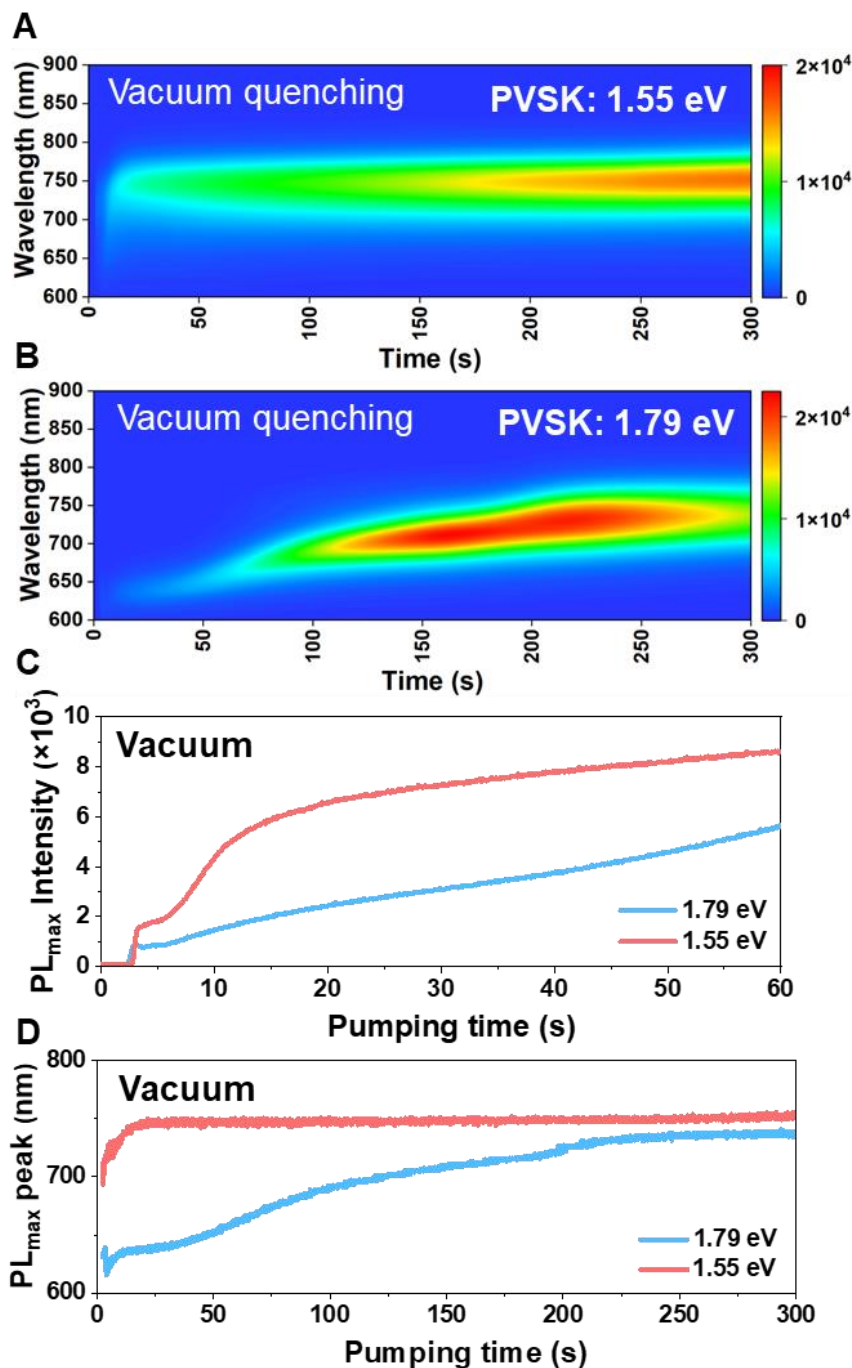
Supplementary Fig. 10. In-situ PL study of different Lewis bases during vacuum quenching. In-situ PL was applied to monitor the nucleation period under vacuum quenching of different precursor solvent systems (A) DMF-DMSO and (B) DMF-NMP. (C) Wavelength variation In-situ PL in A and B. Though NMP (202 °C) has a higher boiling point than DMSO (189 °C), it has a lower donor number ($D_{nDMSO}=29.6$, $D_{nNMP}=27.3$). Step III is the main difference in this comparison group. The NMP sample shows the PL signal first because of its less force with the solute perovskite. Besides, the NMP sample shows the peak at a lower wavelength.



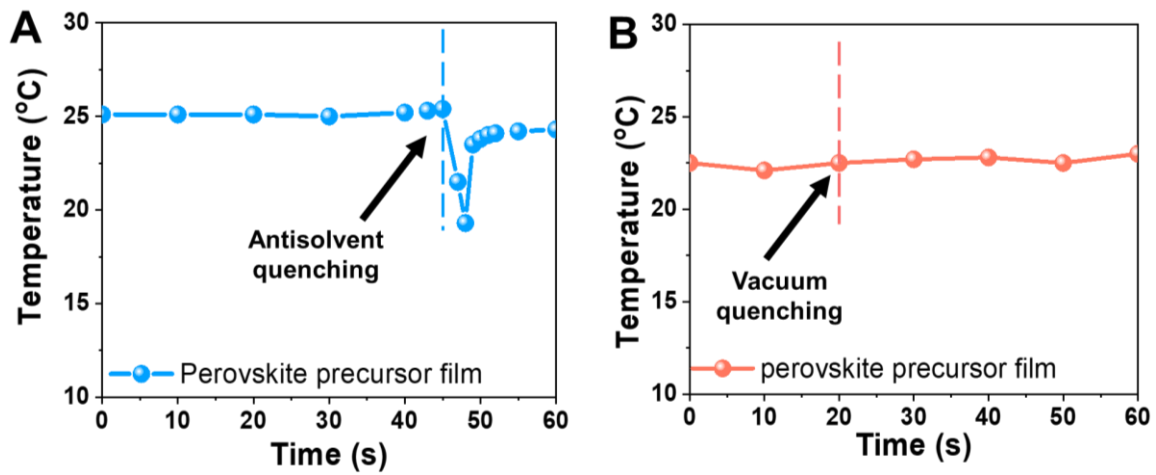
Supplementary Fig. 11. In-situ PL study of different additives during vacuum quenching.

In-situ PL was applied to monitor the influence of additives on the film nucleation under vacuum quenching (A) pristine precursor with no additives, (B) with MACI and (C) with MACI and pF-PEAI. (D) Wavelength variation In-situ PL in A, B, and C. Pristine film shows almost

no peak shift. Meanwhile, the MACl additive dominated the shift of the signal. However, the *p*F-PEAI influences the shift by advancing the peak time and prolonging the step around 710 nm. MACl was helpful for nucleation in previous work.³ We found that those with MACl additive exhibited significantly enhanced signals and shifted from low to high emission wavelength. And with the addition of the *p*F-PEAI additive, the signal occurrence time is advanced. We believe that additives play a role in promoting nucleation in the precursor solution.

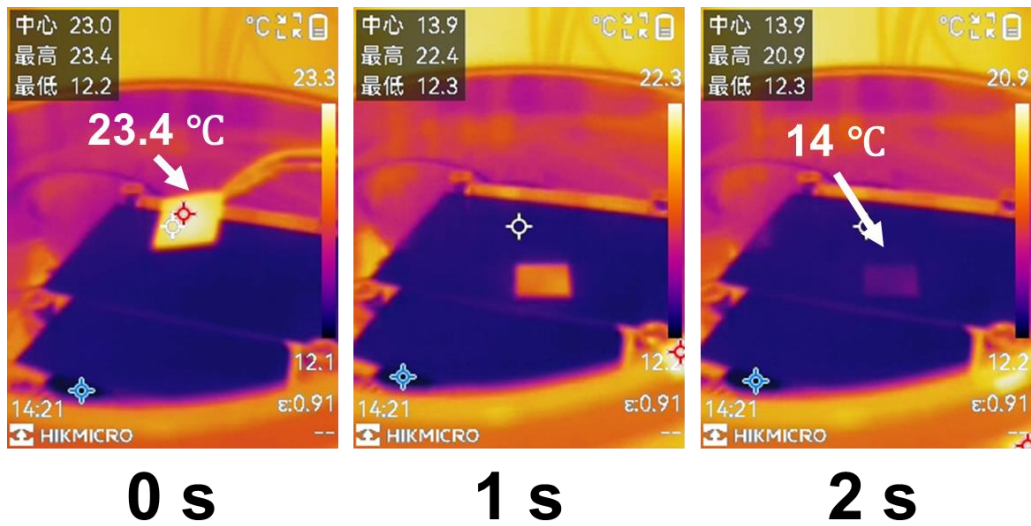


Supplementary Fig. 12. In-situ PL study of different bandgaps. In-situ PL was applied to compare the nucleation of (A) wide band gap perovskite (1.79 eV, $\text{CsPb}(\text{I}_x\text{Br}_{1-x})_3$) and (B) normal band gap perovskite (1.55 eV, $\text{FA}_{0.95}\text{Cs}_{0.05}\text{PbI}_3$) during vacuum quenching. (C) PL intensity variation in A and B. (D) Wavelength variation In-situ PL in A and B. Two bandgaps have the same solvent system of DMF: DMSO = 4:1. They show the PL signal after a similar time gap.

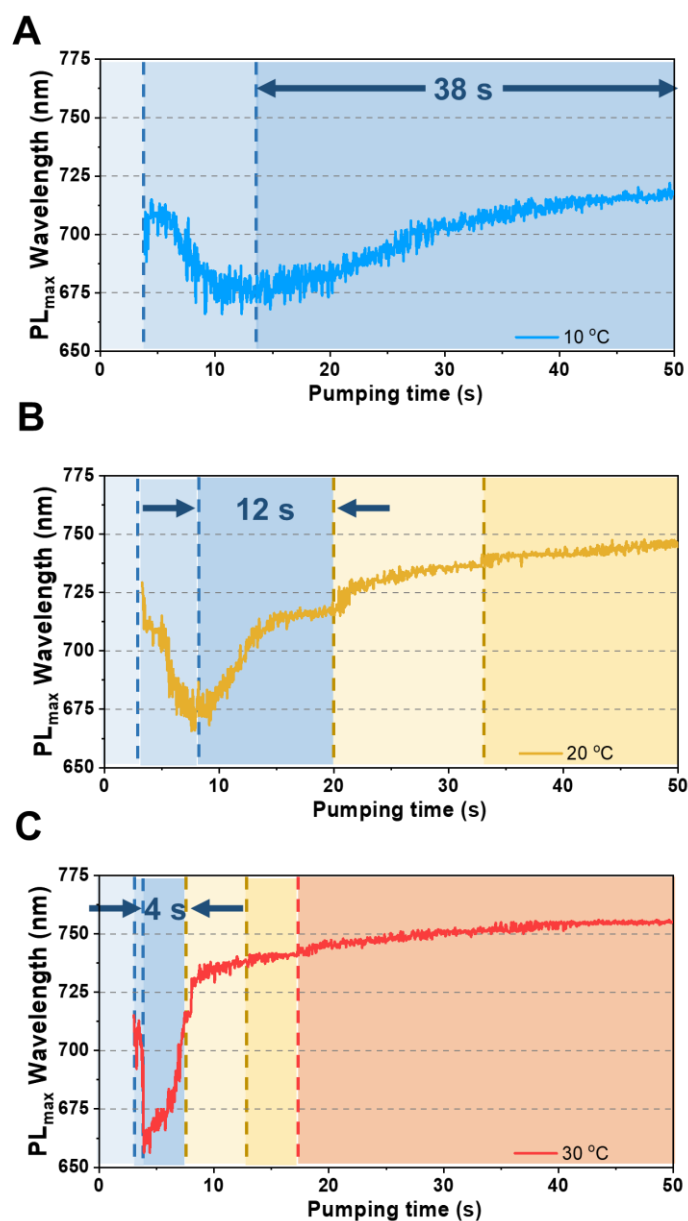


Supplementary Fig. 13. Temperature changes during antisolvent and vacuum quenching.

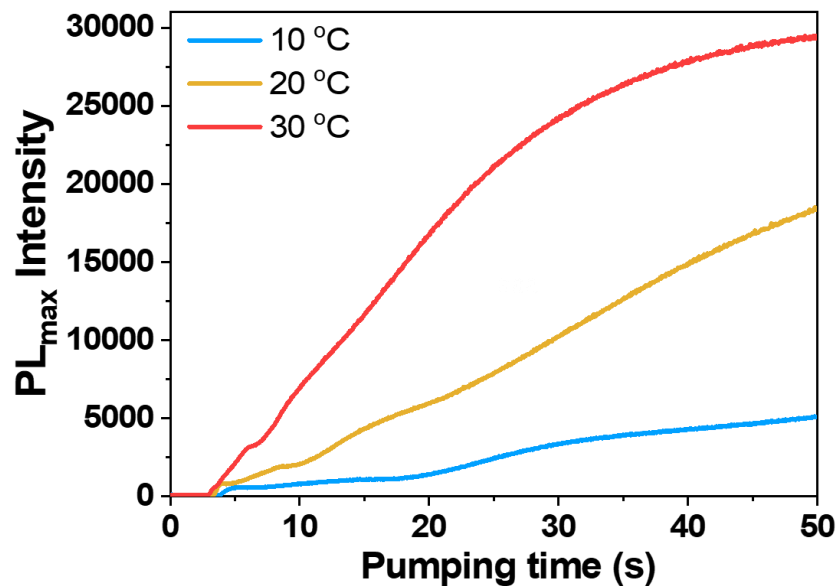
(A) Temperature changes during antisolvent quenching. When the antisolvent was added, the temperature of the film dropped by 6°C within 3 s and then gradually increased to room temperature. (B) Temperature changes during vacuum quenching. The red line is the temperature change of the perovskite precursor film during the vacuum quenching, and the change is minimal.



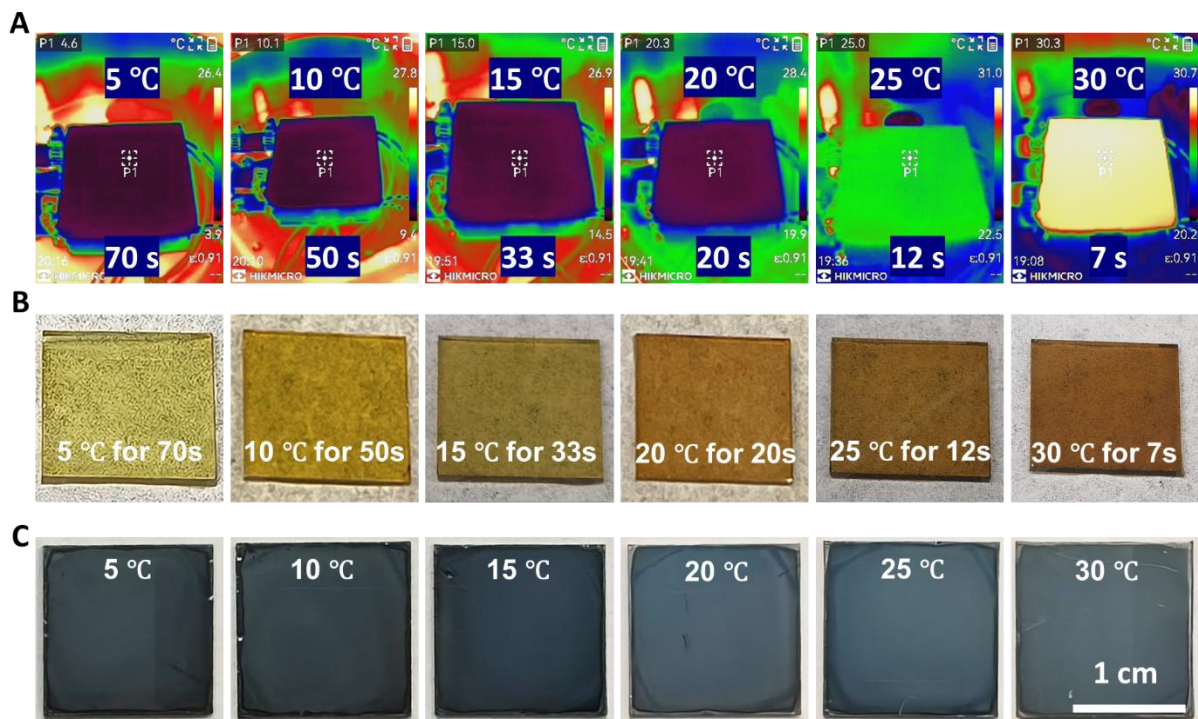
Supplementary Fig. 14. The temperature change of the glass substrate before and after it was placed on the temperature control platform inside the vacuum quenching equipment. Before being placed on the platform, the temperature of the glass substrate was 23.4°C. After contacting the temperature control platform at 13.9°C, within 2 seconds, the temperature of the glass substrate and the temperature control platform were basically consistent. Therefore, the temperature of the film is consistent with the temperature of the temperature control platform at the beginning of vacuum quenching.



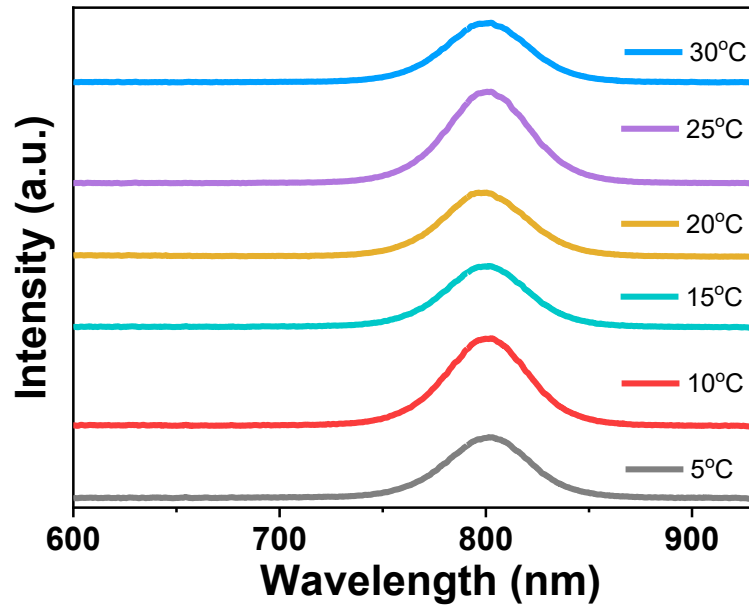
Supplementary Fig. 15. The peak wavelength of in-situ PL changes with time during vacuum quenching at different temperatures. (A-C) The peak wavelength of in-situ PL changes with time during vacuum quenching at different temperatures. (A) 10°C, (B) 20°C, (C) 30°C. The blue interval in the three figures represents the intermediate phase of 675-718 nm. In B and C, the yellow interval represents the intermediate phase of 718-746 nm. The red interval in C represents the intermediate phase of 746-755 nm. Supplementary Table 3 has a more detailed numerical analysis.



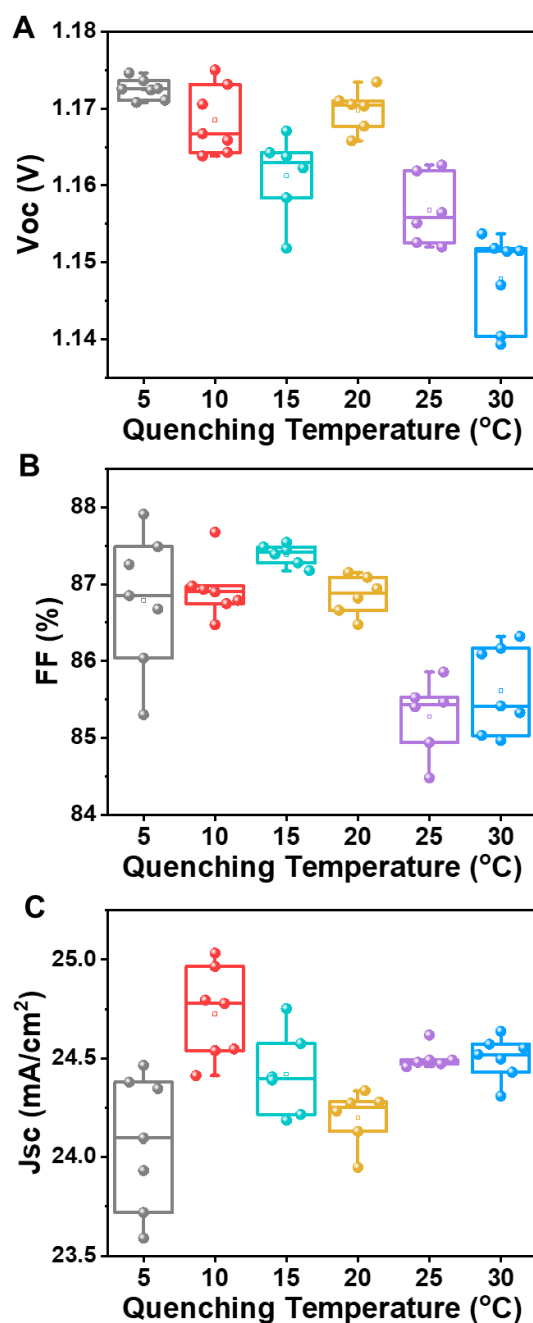
Supplementary Fig. 16. In-situ PL intensity of different temperatures during vacuum quenching of DMF: NMP precursor system. The intensity of in-situ PL was shown to compare the nucleation at different vacuum quenching temperatures (10 °C, 20 °C and 30 °C).



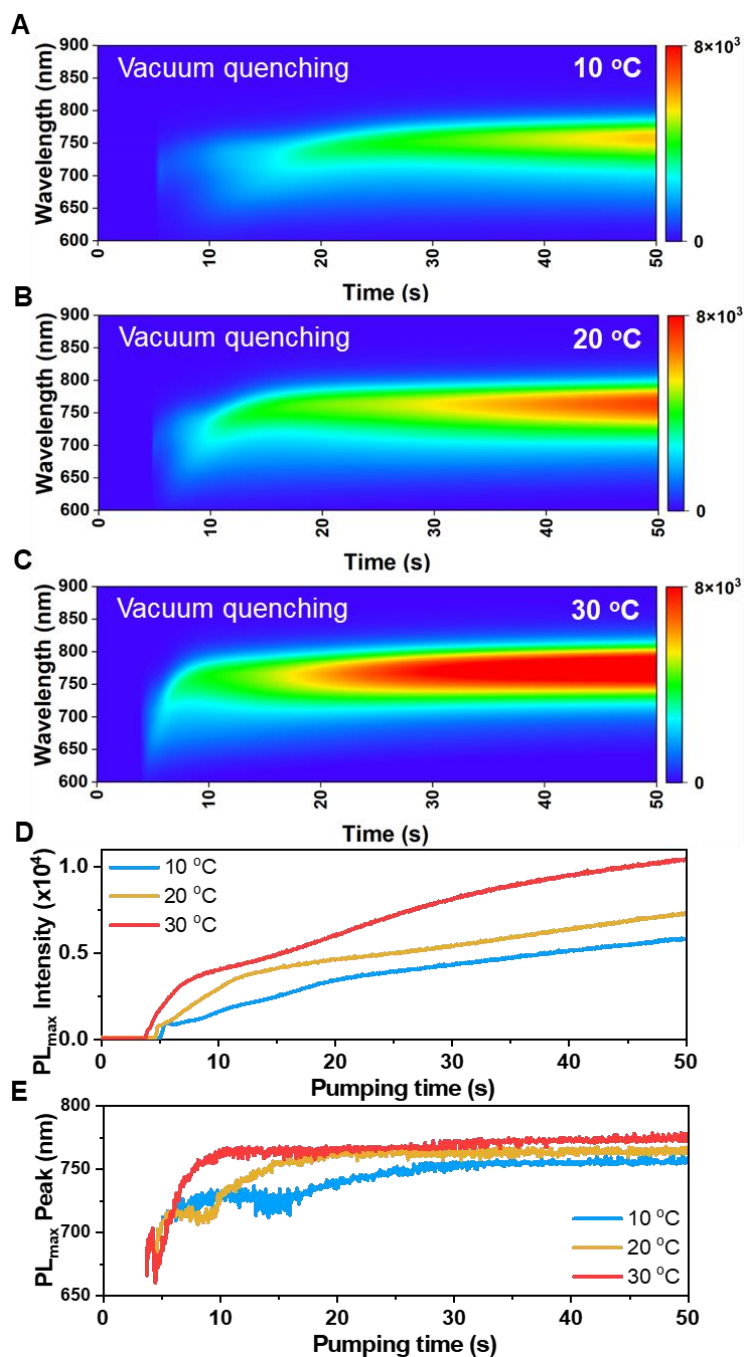
Supplementary Fig. 17. Photos of films obtained by vacuum quenching at different temperatures. (A) Thermal imaging photos of precursor films treated by T-VAQ at different temperatures. (B) Intermediate-phase precursor films after T-VAQ treatment at different temperatures and durations, the treating procedure were: 5 °C for 70s, 10 °C for 50s, 15 °C for 33s, 20 °C for 20s, 25 °C for 12s, 30 °C for 7s and (C) the corresponding optical photos of the films after annealing. During T-VAQ treatments, the in-situ PL was used to monitor the change in the intermediate phase. The T-VAQ treatment was stopped when the PL peak reached a certain wavelength (here, 720 nm was set as the stopping wavelength). Then, these durations were used as the standard treatment durations.



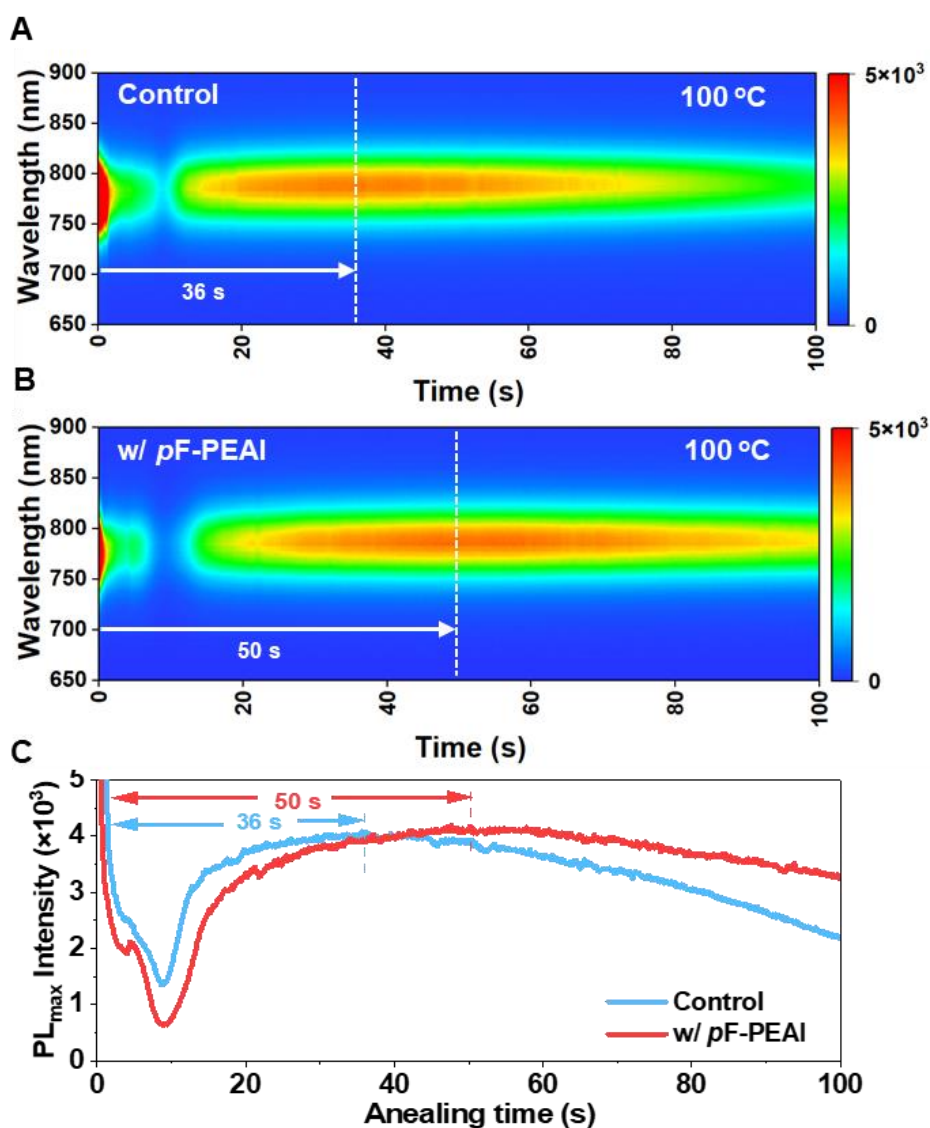
Supplementary Fig. 18. Photoluminescence spectrum of annealed film after different T-VAQ treatments. Similar PL peak positions and peak intensities were observed.



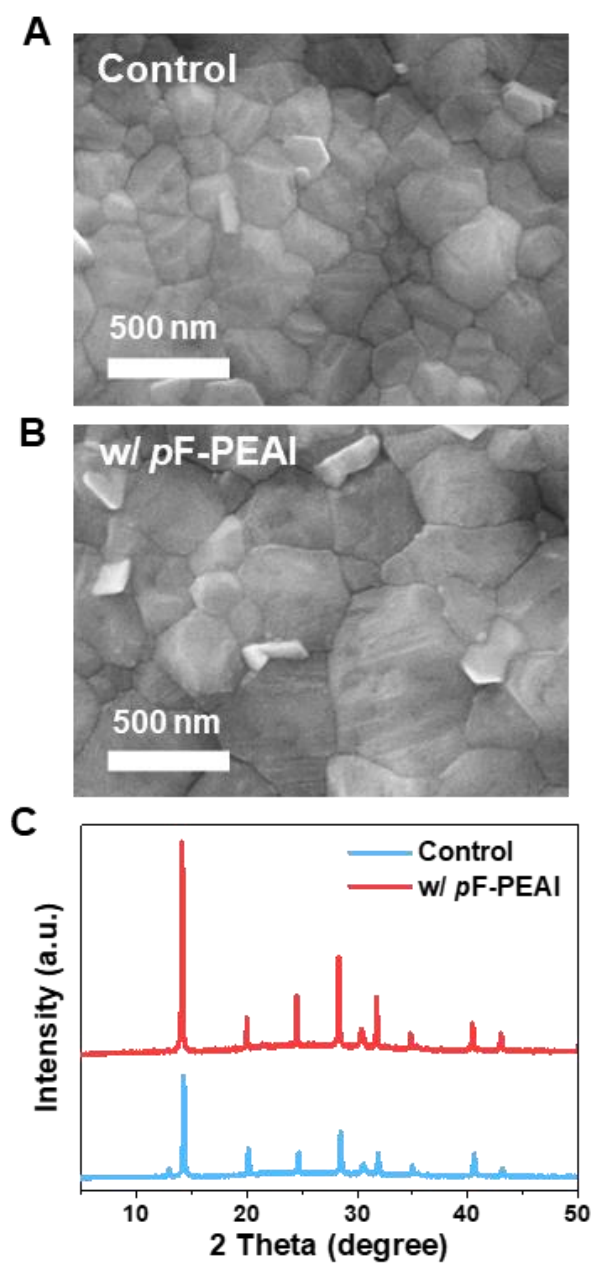
Supplementary Fig. 19. Statistical plots of PSCs at different vacuum quenching temperatures. (A) V_{OC} , (B) FF and (C) J_{SC} of PSCs with an active area of 0.04 cm^2 obtained by T-VAQ at different temperatures. Data from 7 cells were statistically analyzed. The box represents the median and quartiles, and the whisker covers the minimum up to the maximum of the data points. The individual value of each data point is plotted as a point superimposed on the graph.



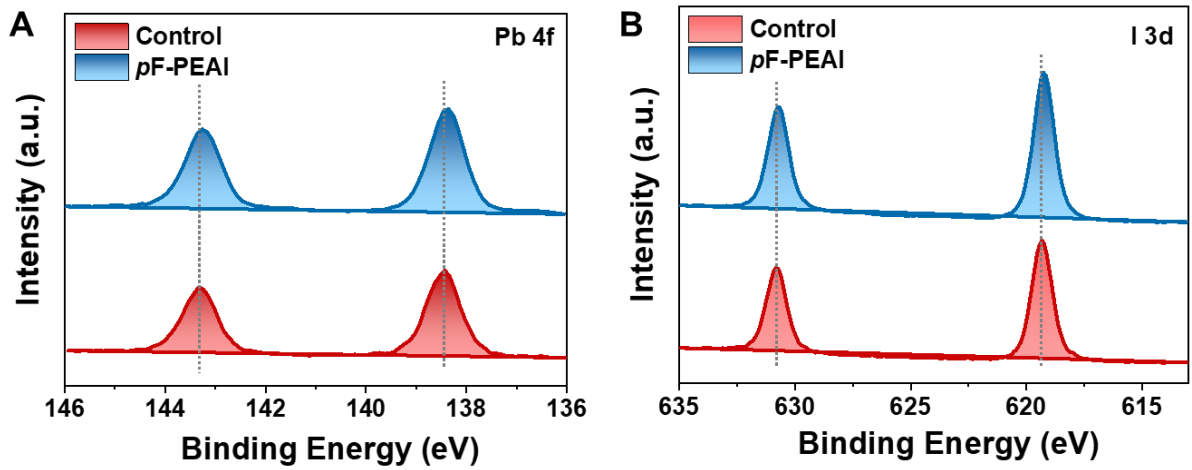
Supplementary Fig. 20. In-situ PL study of different temperatures during vacuum quenching with the DMF: DMSO precursor system. (A-C) In-situ PL was applied to monitor the influence of temperature on the film nucleation under vacuum quenching (A) 10 °C, (B) 20 °C, and (C) 30 °C. (D) PL intensity variation in A, B and C. (E) PL_{max} peak wavelength variation in A, B, and C.



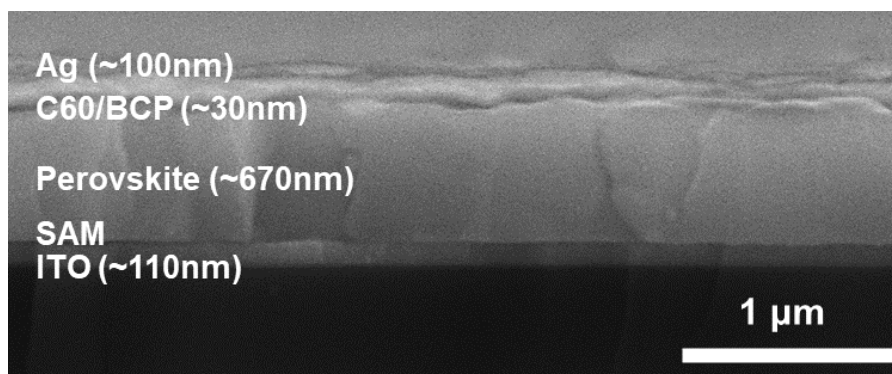
Supplementary Fig. 21. In-situ PL study of control film and film with *p*F-PEAI during annealing. (A) In-situ PL heat map of control film during annealing. (B) target perovskite film with *p*F-PEAI additive during annealing. (C) PL max intensity extracted from PL heat map of control and target film. In-situ PL was applied to monitor the influence of additives on the crystal growth during annealing. The sample with *p*F-PEAI shows a prolonged duration (50 s) to reach the peak of the PL intensity.



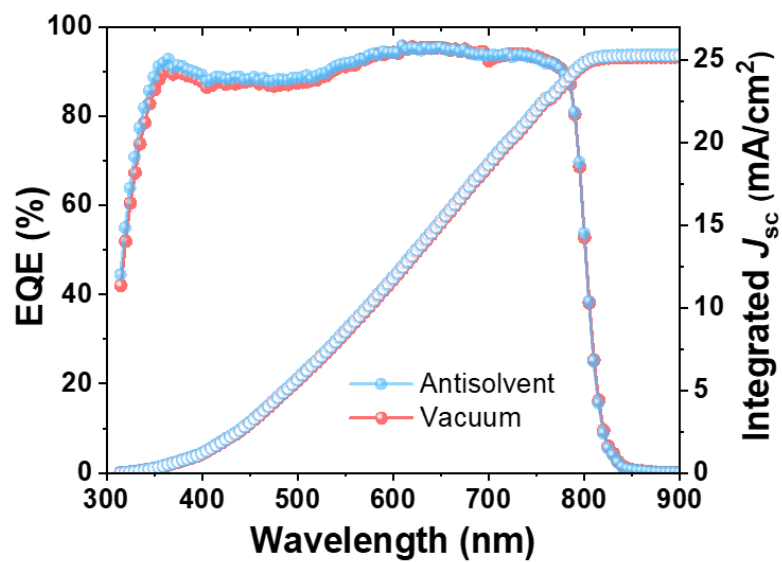
Supplementary Fig. 22. Scanning electron microscope (SEM) of control film and the film with *p*F-PEAI. SEM of annealed (A) control and (B) target perovskite film with *p*F-PEAI additive perovskite film. (C) XRD patterns of the control and target films.



Supplementary Fig. 23. X-ray photoelectron spectroscopy (XPS) study of control film and the film with *p*F-PEAI. (A) Pb 4f spectra of control film and the film with *p*F-PEAI. (B) I 3d spectra of the control film and the film with *p*F-PEAI. XPS peak shift to lower binding energy after the addition of *p*F-PEAI, indicating that the additive interacts with the perovskite film.

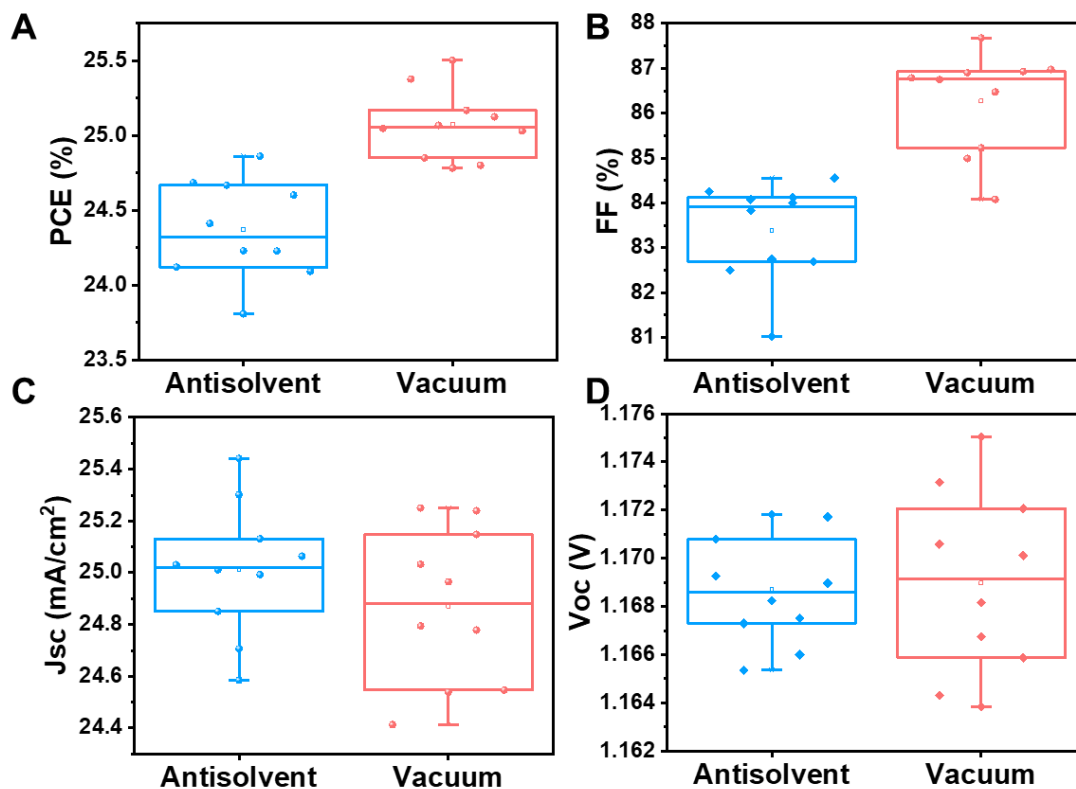


Supplementary Fig. 24. SEM images of the cross-section of the PSM. SEM images showing the full stack of PSCs based on vacuum quenching. The thickness of perovskite, C60 and Ag electrode are around 670 nm, 30 nm and 100 nm, respectively. The SAM-based HTL is indistinguishable.

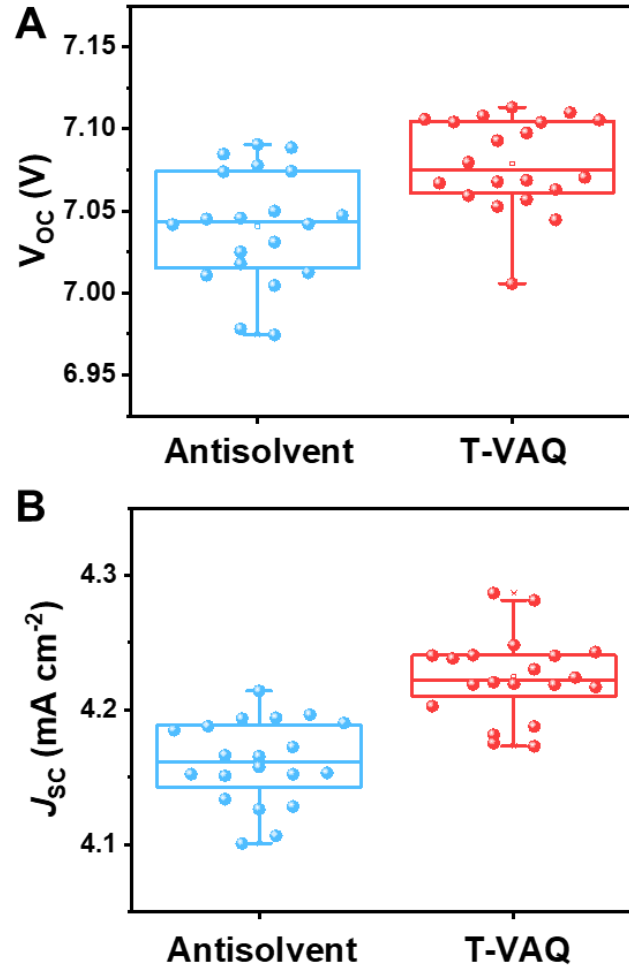


Supplementary Fig. 25. EQE of perovskite solar cell. The antisolvent-treated PSC is 25.26

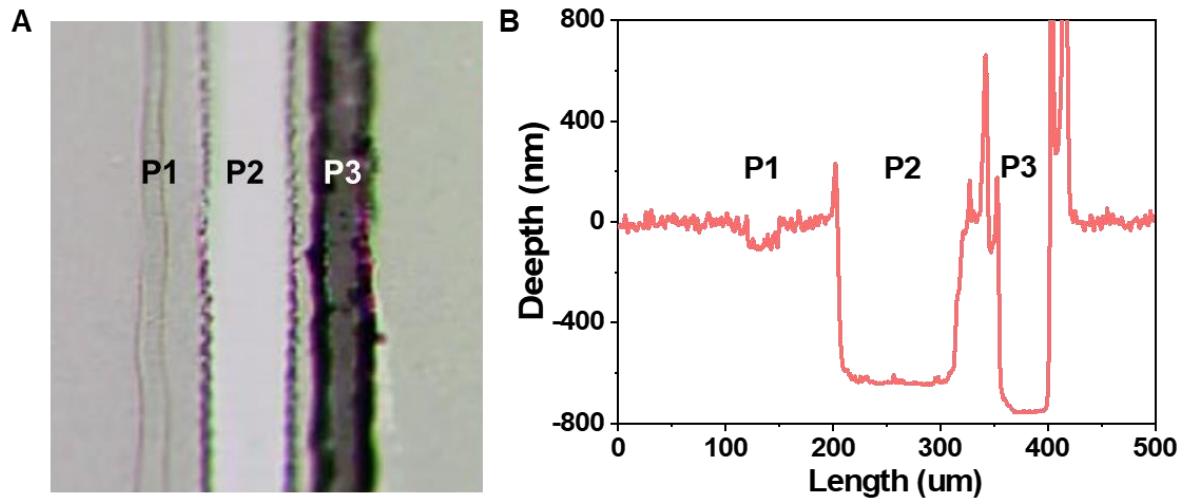
mA cm⁻² and the integrated J_{sc} of the T-VAQ-treated cell is 25.17 mA cm⁻²



Supplementary Fig. 26. Statistical plots of PSCs at antisolvent and vacuum quenching methods. Statistic photovoltaic parameters of the antisolvent quenching and T-VAQ-based cells in 10 devices with an active area of 0.04 cm². (A) PCE, (B) FF, (C) J_{sc} , (D) V_{oc} . The box represents the median and quartiles, and the whisker covers the minimum up to the maximum of the data points. The individual value of each data point is plotted as a point superimposed on the graph.



Supplementary Fig. 27. Statistical plots of PSMs at antisolvent and vacuum quenching methods. Statistic photovoltaic parameters of the antisolvent quenching and T-VAQ-based mini-modules in 20 devices with an active area of 11.0 cm². (A) V_{oc} , (B) J_{sc} . The box represents the median and quartiles, and the whisker covers the minimum up to the maximum of the data points. The individual value of each data point is plotted as a point superimposed on the graph.



Supplementary Fig. 28. Laser patterning of the PSM. The ITO substrate was patterned for P1 (25 μm wide). The P2 lines (125 μm wide) were patterned using overlapped 2 lines. After Ag layers were sequentially deposited, the P3 lines (65 μm wide) were patterned. The distance between the P1 and P3 lines is about 300 μm and the geometric fill factor (GFF) is 94%.



中国认可
国际互认
检测
TESTING
CNAS L8490

Test and Calibration Center of New Energy Device and Module,
Shanghai Institute of Microsystem and Information Technology,
Chinese Academy of Sciences (SIMIT)

Measurement Report

Report No. 24TR051401

Client Name	Prof. Alex K.-Y. Jen's Research Group
Client Address	City University of Hong Kong, Kowloon Tong, Hong Kong SAR
Sample	Perovskite PV mini-module
Manufacturer	City University of Hong Kong
Measurement Date	14 th May, 2024

Performed by:	Qiang Shi <i>Qiang Shi</i>	Date: 14/05/2024
Reviewed by:	Wenjie Zhao <i>Wenjie Zhao</i>	Date: 14/05/2024
Approved by:	Yucheng Liu <i>Yucheng Liu</i>	Date: 14/05/2024



Address: No.235 Chengbei Road, Jiading, Shanghai	Post Code: 201800
E-mail: solarcell@mail.sim.ac.cn	Tel: +86-021-69976905

The measurement report without signature and seal are not valid.
This report shall not be reproduced, except in full, without the approval of SIMIT.



Sample Information	
Sample Type	Perovskite PV mini-module
Serial No.	8-1-2
Lab Internal No.	24051401-1#
Measurement Item	I-V characteristic
Measurement Environment	24.3 ± 2.0°C, 40.5 ± 5.0%R.H

Measurement of I-V characteristic	
Reference cell	PVM1121
Reference cell Type	mono-Si, WPVS, calibrated by NREL (Certificate No. ISO 2098)
Calibration Value/Date of Calibration for Reference cell	143.95mA/ Feb. 2024
Measurement Conditions	Standard Test Condition (STC): Spectral Distribution: AM1.5 according to IEC 60904-3 Ed.3, Irradiance: 1000 ± 50W/m ² , Temperature: 25 ± 2°C
Measurement Equipment/ Date of Calibration	AAA Steady State Solar Simulator (YSS-T155-2M) / July.2023 IV test system (ADCMT 6246) / June. 2023 Measuring Microscope (MF-B2017C) / July.2023 SR Measurement system (CEP-25ML-CAS) / May.2024
Measurement Method	I-V measurement: Logarithmic sweep in both directions (Voc to Isc and Isc to Voc) during one flash based on IEC 60904-1:2020. Spectral Mismatch factor was calculated according to IEC 60904-7 and I-V correction according to IEC 60891.
Measurement Uncertainty	Area:0.5%; Isc: 2.0%(k=2); Voc: 1.0%(k=2); Pmax: 2.4%(k=2); Eff:2.5%(k=2)

====Measurement Results====

	Forward Scan (Isc to Voc)	Reverse Scan (Voc to Isc)
Area	11.7077 cm ²	
Isc	45.277 mA	45.308 mA
Voc	7.044 V	7.101 V
Pmax	239.268 mW	252.928 mW
Ipm	40.123 mA	42.065 mA
Vpm	5.963 V	6.013 V
FF	75.02 %	78.61 %
Eff	20.44 %	21.60 %

- Spectral Mismatch Factor: SMM=0.9960.
- Designated illumination area defined by a thin mask was measured by measuring microscope.
- Test results listed in this measurement report refer exclusively to the mentioned measured sample.
- The results apply only at the time of the test, and do not imply future performance.

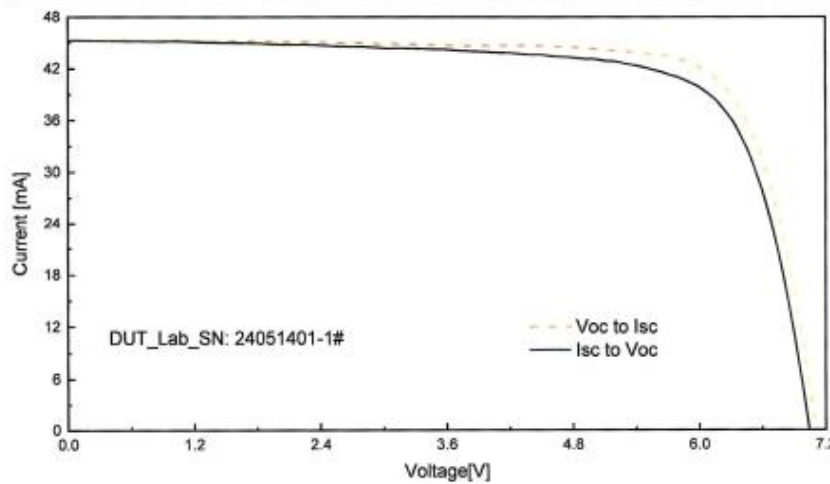
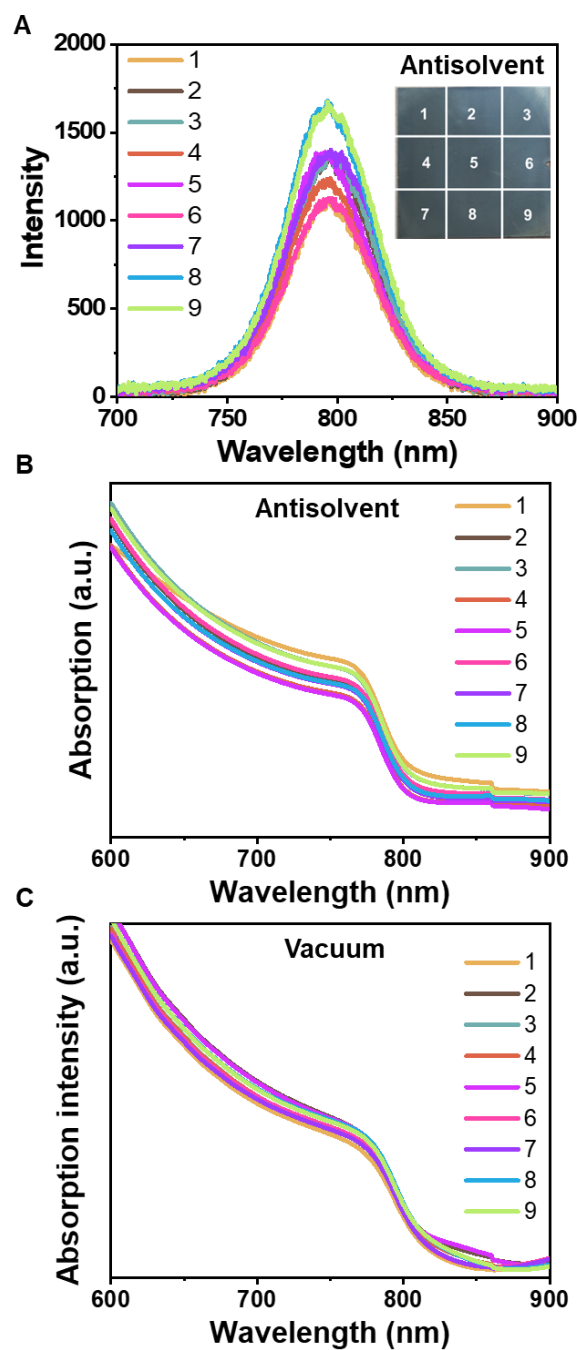


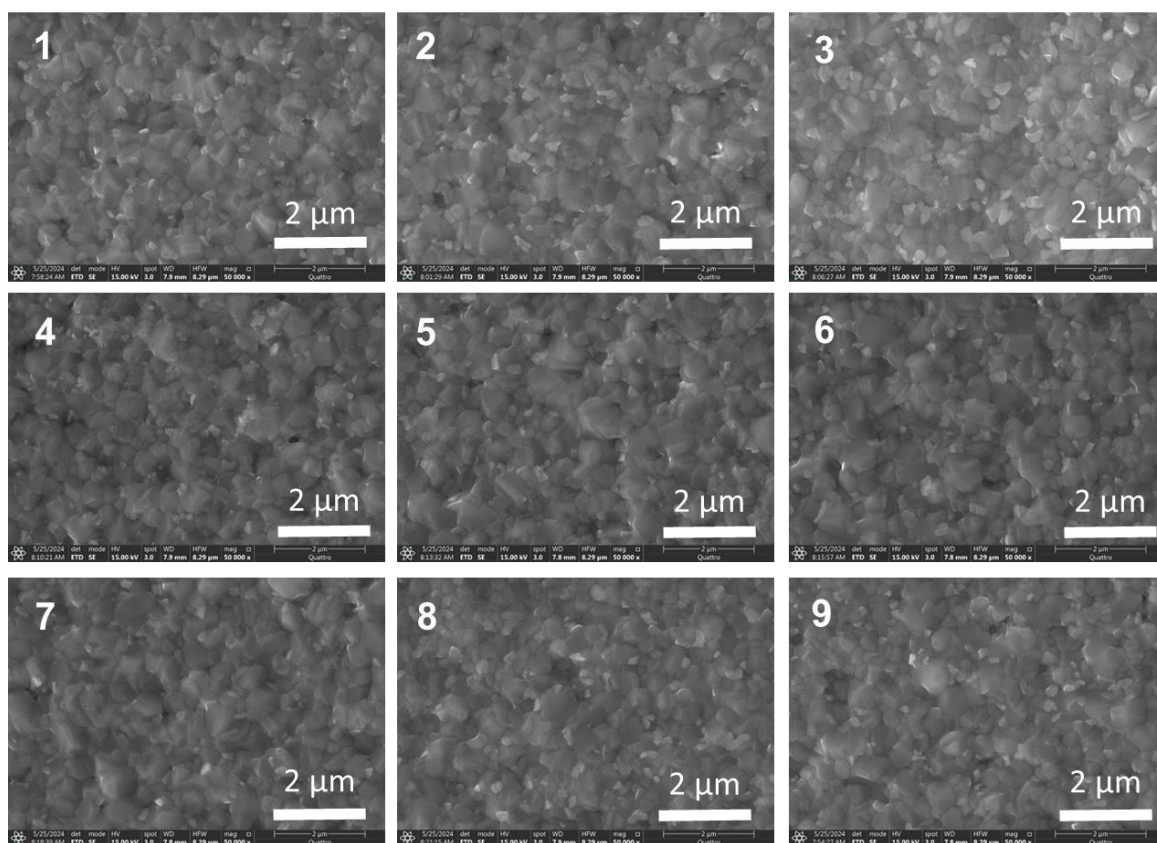
Fig.1 I-V curves of the measured sample

Supplementary Fig. 29. Certification report. Certification report of the target module based on the vacuum quenching nucleation method by the Shanghai Institute of Microsystem and Information Technology (SIMIT). The certified aperture-area PCE is 21.60% under reverse scan (short-circuit current (I_{SC}) of 45.308 mA, V_{OC} of 7.101 V and FF of 78.61%), which is equal to an active-area PCE of 22.98% with an active area of 11.0 cm² and a GFF of 94%.

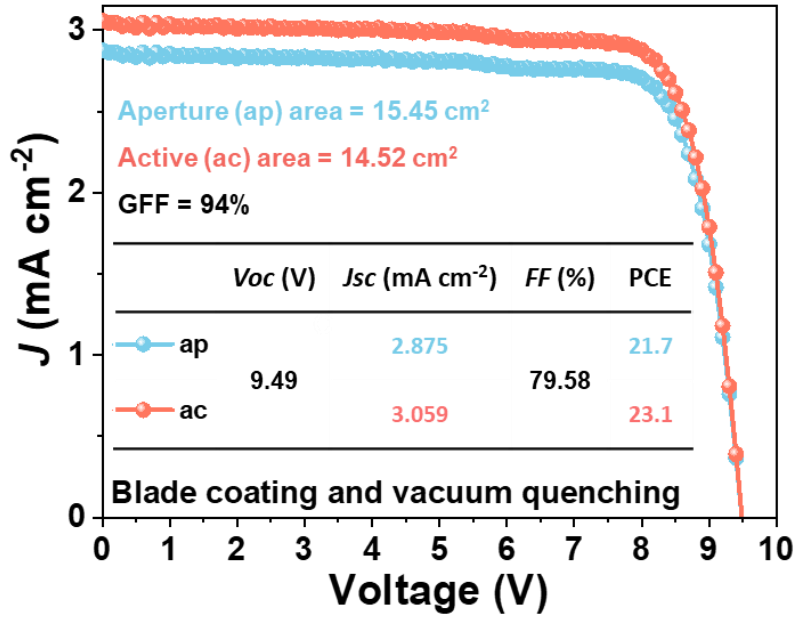


Supplementary Fig. 30. Uniformity test of antisolvent and T-VAQ treated film by PL and UV. Divide the $5 \times 5 \text{ cm}^2$ film into nine parts and conduct PL and UV testing separately. (A) The PL of the antisolvent quenched film is showing a noticeable change. Insert is the picture of an antisolvent quenched film. (B, C) The UV-Vis absorption spectrum of the film treated by (B) antisolvent and (C) T-VAQ methods, respectively. The results show that the vacuum-quenched film shows better uniformity.

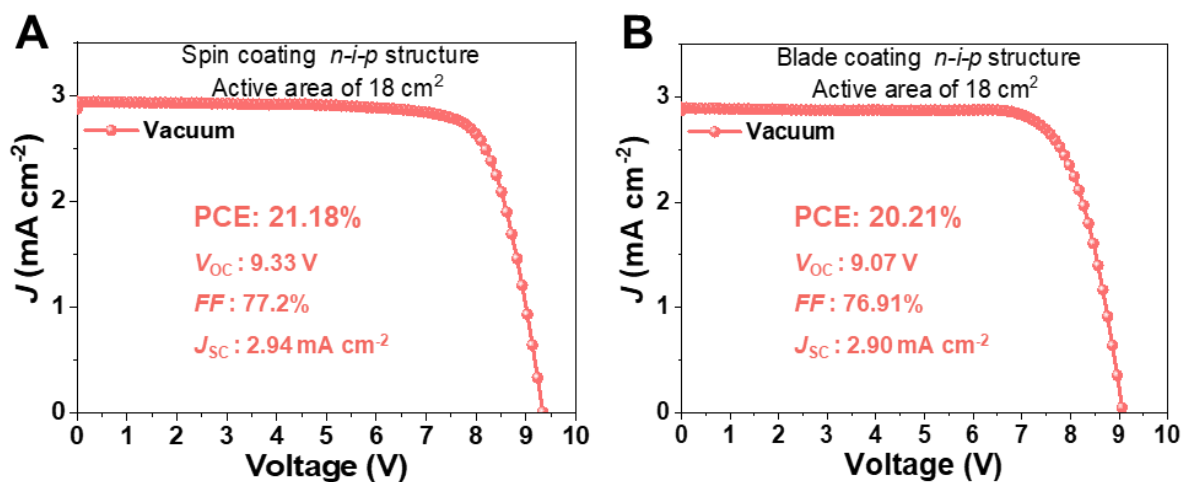
Vacuum quenching



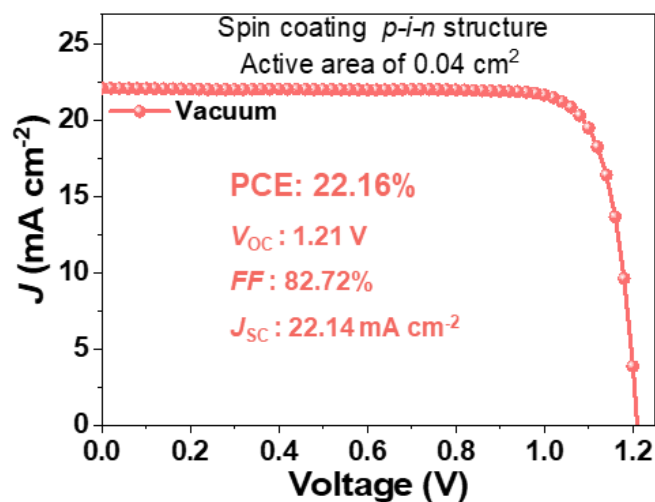
Supplementary Fig. 31. Uniformity of T-VAQ treated film by SEM. Divide the $5 \times 5 \text{ cm}^2$ film into nine parts and conduct SEM testing on them separately. The results show that the film in the nine parts is relatively uniform.



Supplementary Fig. 32. *J-V* of *p-i-n* structure mini-module with the perovskite film fabricated by a blade-coating and T-VAQ method. The module was based on the 5 × 5 cm² substrate, with 8 subcells. The active-area PCE is 23.1% with an active area of 14.52 cm² and a GFF of 94% under reverse scan (J_{SC} of 3.059 mA cm⁻², V_{OC} of 9.486 V and FF of 79.58%).



Supplementary Fig. 33. *J-V* of *n-i-p* structured mini-module with the perovskite film fabricated by vacuum quenching method. (A) *J-V* of spin-coated *n-i-p* structure mini-module. The PCE is 21.18% (J_{SC} of 2.94 mA cm⁻², V_{OC} of 9.33 V and FF of 77.2%). The module was based on the 6 × 6 cm² substrate, with 8 subcells and an active area of 18 cm². (B) *J-V* of blade-coated *n-i-p* structure mini-module. The PCE is 20.21% (J_{SC} of 2.90 mA cm⁻², V_{OC} of 9.07 V and FF of 76.91%).



Supplementary Fig. 34. *J-V* of *p-i-n* structured wide-bandgap PSCs with the perovskite film fabricated by vacuum quenching method. *J-V* of spin-coated wide band gap (1.67 eV) *p-i-n* structure solar cell with an active area of 0.04 cm². The composition is FA_{0.8}CS_{0.2}Pb(I_{0.8}Br_{0.2})₃. The PCE is 22.16% (*J*_{SC} of 22.14 mA cm⁻², *V*_{OC} of 1.21 V and *FF* of 82.72%).

Supporting Tables.

Supplementary table 1. Quantitative evaluation of three quenching methods: antisolvent, vacuum, and gas quenching.

	Antisolvent quenching	Vacuum quenching	Gas quenching
Quenching capacity	10 Very fast. Relatively hard to control.	8 Tunable according to pumping speed	4 Relatively slow
reproducibility	6 The precursor solution that enters the anti-solvent tank during quenching dilutes the anti-solvent, changing its concentration with each quenching treatment. This variation can affect the reproducibility of the process.	9 The vacuum quenching process has fewer variable factors, thus showing higher reproducibility.	4 The pressure generated by the airflow can significantly impact the surface uniformity of the precursor film. Since airflow is challenging to control, this leads to reduced repeatability.
environmental impact	3 Commonly used anti-solvents are mostly organic solvents, adversely affecting the environment and the human body. The use of green solvents can help improve this problem.	9 The organic solvent in the precursor solution is absorbed into the vacuum tank at the rear end or can be captured using a cold trap or other methods, making the control of organic solvents during vacuum quenching highly manageable.	6 The organic solvent in the precursor is dispersed into the air near the equipment during air quenching, posing challenges for collecting large volumes of air and potentially causing harm to human health.
Equipment and maintenance costs	7 Solvent tanks and purification equipment are necessary, and the continuous input of organic solvents during ongoing operations will incur substantial costs.	7 Vacuum quenching equipment is necessary, with a relatively high initial investment; electricity is the primary ongoing operational cost.	8 An air knife and compressed air equipment are needed, with an initial investment slightly lower than vacuum quenching. The main ongoing costs include

			electricity and compressed gas.
	6	7	8
Scalability	Scaling up can be achieved by using a sizeable liquid tank, and it can also be integrated into roll-to-roll equipment.	Scaling up can be accomplished by using a large vacuum chamber, and it can also be integrated into roll-to-roll equipment.	Scaling up can be achieved by using a longer air knife, and it can also be integrated into roll-to-roll equipment.
Sum	32	40	30

Supplementary table 2. Antoine coefficients of solvents widely used in perovskite photovoltaics.

	A	B	C	T_{min} (°C)	T_{max} (°C)
2-Methoxyethanol (2-ME)	8.09715	1805.18	221.663	-85.1	290.85
N,N-Dimethylformamide (DMF)	7.24128	1597.92	213.457	-60.43	373.85
γ-butyrolactone (GBL)	7.67415	2147.61	244.041	-43.37	465.85
dimethyl sulfoxide (DMSO)	7.25197	1733.52	207.58	18.52	452.85
N-methyl-2-pyrrolidone (NMP)	7.36115	1869.62	215.294	-24	450.85
Acetonitrile (ACN)	7.54662	1583.98	257.887	-43.83	272.35
Acetone (ACE)	7.31414	1315.67	240.479	-94.7	235.05

Supplementary table 3. Donor number and boiling point of different main solvents.

	2-ME	DMF	GBL	NMP	DMSO
Donor number kcal/mol	19.8	26.6	18	27.3	29.8
Boiling point °C	124	153	204	202	189

Supplementary table 4. Wavelength variation of in-situ PL of vacuum quenching at different temperatures.

Wavelength	10 °C		20 °C		30 °C			
	<i>t</i> (s)	Δt (s)	<i>t</i> (s)	Δt (s)	<i>t</i> (s)	Δt (s)		
Appear	3.8	3.8	3.3	3.3	2.9	2.9		
675 nm	11.6	7.8	7.7	4.4	4.2	1.3		
718 nm	50	38.4	20.1	12.4	7.9	3.7		
736 nm			32.9	29.7	12.9	9.4		
746 nm			50		17.3			
755 nm							38.7	32.7
stable							50	

Supplementary table 5. Statistic photovoltaic parameters of the T-VAQ-based PSCs at different temperatures with an active area of 0.04 cm².

T-VAQ (°C)	<i>V_{oc}</i> (V)	<i>J_{sc}</i> (mA cm ⁻²)	<i>FF</i> (%)	<i>PCE</i> (%)
30	1.139	24.64	86.32	24.24
	1.148±0.006	24.50±0.11	85.62±0.56	24.09±0.16
25	1.162	24.62	85.46	24.45
	1.157±0.005	24.50±0.06	85.28±0.49	24.17±0.22
20	1.170	24.34	87.09	24.80
	1.170±0.003	24.20±0.14	86.86±0.26	24.58±0.13
15	1.158	24.75	87.48	25.08
	1.161±0.005	24.42±0.22	87.39±0.14	24.78±0.26
10	1.175	24.97	86.98	25.50
	1.169±0.004	24.72±0.23	86.93±0.37	25.11±0.26
5	1.175	24.46	86.85	24.95
	1.173±0.001	24.08±0.34	86.79±0.89	24.49±0.26

Supplementary table 6. Statistic photovoltaic parameters of the antisolvent and T-VAQ-based solar cells (0.04 cm²) and mini-modules (11.0 cm²).

		V_{oc} (V)	J_{sc} (mA cm ⁻²)	FF (%)	PCE (%)
Solar Cell	Antisolvent	1.168	25.30	84.12	24.86
		1.169±0.002	25.01±0.255	83.38±1.105	24.37±0.330
	T-VAQ	1.175	24.97	86.98	25.50
		1.169±0.004	24.87±0.304	86.28±1.124	25.08±0.236
Mini-module	Antisolvent	7.091	4.16	77.73	22.93
		7.041±0.035	4.16±0.031	77.93±0.829	22.81±0.101
	T-VAQ	7.093	4.20	80.97	24.14
		7.079±0.028	4.22±0.031	79.25±0.973	23.72±0.291

Supplementary table 7. Width of Sub-cell and each laser scribing of the PSMs.

	Subcell	P1	P1-P2	P2	P2-P3	P3	SUM	GFF
Width	5 mm	25 μm	50 μm	125 μm	25 μm	65 μm	300 μm	94%

Reference

1. Petrov, A.A., Ordinartsev, A.A., Fateev, S.A., Goodilin, E.A. & Tarasov, A.B. Solubility of Hybrid Halide Perovskites in DMF and DMSO. *Molecules* **26** (2021).
2. Kim, J.Y. et al. Efficient Tandem Polymer Solar Cells Fabricated by All-Solution Processing. *Science* **317**, 222-225 (2007).
3. Bi, L. et al. Deciphering the Roles of MA-Based Volatile Additives for alpha-FAPbI(3) to Enable Efficient Inverted Perovskite Solar Cells. *J Am Chem Soc* **145**, 5920-5929 (2023).